THE ASTROPHYSICAL JOURNAL, 519:134–152, 1999 July 1

HUBBLE SPACE TELESCOPE FAINT OBJECT CAMERA SPECTROSCOPY OF THE NARROW-LINE REGION OF NGC 4151. I. GAS KINEMATICS[1]

CLÁUDIA WINGE,[2,3] DAVID J. AXON,[4,5] AND F. D. MACCHETTO[4]
Space Telescope Science Institute, 3700 San Martin Drive, Baltimore, MD 21218

A. CAPETTI
Osservatorio Astronomico di Torino, Strada Osservatorio 20, 10025 Pino Torinese, Torino, Italy

AND

A. MARCONI
Osservatorio Astrofisico di Arcetri, Largo E. Fermi 5, 50125 Firenze, Italy
Received 1998 May 7; accepted 1999 February 5

ABSTRACT

We present the results from a detailed kinematic analysis of both ground-based, and *Hubble Space Telescope* (*HST*)/Faint Object Camera long-slit spectroscopy at subarcsecond spatial resolution of the narrow-line region (NLR) of NGC 4151. In agreement with previous work, the extended emission gas ($R > 4''$) is found to be in normal rotation in the galactic plane, a behavior that we were able to trace even across the nuclear region, where the gas is strongly disturbed by the interaction with the radio jet and connects smoothly with the large-scale rotation defined by the neutral gas emission. The *HST* data, at 0ʺ029 spatial resolution, allow us for the first time truly to isolate the kinematic behavior of the individual clouds in the inner narrow-line region. We find that, underlying the perturbations introduced by the radio ejecta, the general velocity field can still be well represented by planar rotation down to a radius of ∼0ʺ5 (30 pc), the distance at which the rotation curve has its turnover. The most striking result that emerges from our analysis is that the galaxy potential derived fitting the rotation curve changes from a "dark halo" at the extended narrow-line region distances to being dominated by the central mass concentration in the NLR, with an almost Keplerian falloff in the $1'' < R < 4''$ interval. The observed velocity of the gas at 0ʺ5 implies a mass of $M \sim 10^9\ M_\odot$ within the inner 60 pc. The presence of a turnover in the rotation curve indicates that this central mass concentration is extended. The first measured velocity point (outside the region saturated by the nucleus) would imply an enclosed mass of $\sim 5 \times 10^7\ M_\odot$ within $R \sim$ 0ʺ15 (10 pc), which represents an upper limit to any nuclear point mass.

Subject headings: galaxies: individual (NGC 4151) — galaxies: kinematics and dynamics — galaxies: Seyfert

1. INTRODUCTION

The SABab galaxy NGC 4151 hosts one of the most studied active galactic nuclei (AGN) in the sky, with observations from the γ-ray to the MHz range (see, e.g., Kriss et al. 1995; Knop et al. 1996; Warwick et al. 1996; Ulvestad et al. 1998). The AGN spectrum presents a broad X-ray Fe Kα line (Yaqoob et al. 1995) and optical and UV variable broad permitted emission lines (Crenshaw et al. 1996; Kaspi et al. 1996), as well as several blueshifted narrow absorption systems (Weymann et al. 1997) and strong narrow lines that originated in a system of clouds with an extension of up to a few kiloparsecs (Pérez et al. 1989; Yoshida & Ohtani 1993). The extended narrow-line region (ENLR) of NGC 4151 shows line intensities and widths as well as kinematics consistent with quiescent gas in normal rotation in the galactic disk, illuminated by the central source (Penston et al. 1990; Robinson et al. 1994). Several authors have remarked on the continuity between the kinematics of the large-scale H I 21 cm emission and that of the ENLR (Vila-Vilaró et al. 1995; Asif et al. 1997), but because of the contamination by the narrow-line region (NLR; $R < 4''$), the ground-based data have not yielded convincing evidence for normal rotation in the circumnuclear region of NGC 4151 (Schulz 1987; Mediavilla, Arribas, & Rasilla 1992).

Narrowband *Hubble Space Telescope* (*HST*) images (Evans et al. 1993; Boksenberg et al. 1995) suggested that the complex morphology of the emission clouds and filaments in the NLR ($R < 4''$) is shaped not by the anisotropic character of the central source's radiation but mainly by the interaction between the hot plasma of the radio jet and the ambient gas in the disk. In a previous paper (Winge et al. 1997, hereafter Paper I), we presented the initial results from *HST* long-slit spectroscopy of the NLR of NGC 4151 at a spatial resolution of 0ʺ029, isolating for the first time the spectra of individual clouds and demonstrating the influence of the radio ejecta in both the local kinematic and ionization conditions of the emission gas. Several very localized subsystems of both blue- and redshifted high-velocity knots were detected, and we also observed off-nuclear continuum emission and marked variations on the emission-line ratios within a few parsecs. Such evidence indicates that the physical conditions of the emission gas in individual clouds are strongly influenced by local parameters, either density fluctuations or shock ionization, possibly both.

---

[1] Based on observations made with the NASA/ESA *Hubble Space Telescope*, obtained at the Space Telescope Science Institute, which is operated by the Association of Universities for Research in Astronomy, Inc., under NASA contract NAS 5-26555.

[2] CNPq Fellowship, Brazil; winge@if.ufrgs.br.

[3] Current address: Instituto de Física, Universidade Federal do Rio Grande do Sul, Av. Bento Gonçalves, 9500, C.P. 15051, CEP 91501-950, Porto Alegre, RS, Brazil.

[4] Affiliated to the Space Science Department of ESA.

[5] Division of Physical Sciences, University of Hertfordshire, College Lane, Hatfield, Herts, AL10 9AB, U.K.

In this paper we present a detailed study of the kinematics of the gas in both the extended and inner NLR of NGC 4151 from ground-based and *HST* data with high spatial resolution that allow us to separate the underlying velocity field of the emission gas in the NLR from the effects of the radio jet and to probe its connection with the large-scale rotation of the ENLR in the galactic disk. The most striking evidence for the interaction of the radio jet with the ambient gas and the presence of strong shocks, observed as high-velocity emission knots, localized off-nuclear continuum emission, and variations in the emission-line ratios in scales of a few to tens of parsecs, will be discussed in a forthcoming paper.

For a distance to NGC 4151 of 13.3 Mpc, 0″.1 corresponds to a linear scale of 6.4 pc in the plane of the sky; a value of $H_0 = 75$ km s^{-1} Mpc^{-1} is assumed throughout this paper.

2. OBSERVATIONS AND DATA REDUCTION

2.1. *Ground-based Data*

Long-slit spectroscopic observations of NGC 4151 were obtained using the IPCS (Boksenberg 1972; Boksenberg & Burgess 1973) at the f/15 Cassegrain focus of the 2.5 m Isaac Newton Telescope on 1985 March 9–13. The wavelength coverage includes the [O III] $\lambda\lambda$4959, 5007 and Hβ lines, at an instrumental resolution of 0.75 Å (45 km s^{-1}) full width half-maximum (FWHM). The spatial resolution was 0″.63. A total of 17 spectra were obtained at PA = 48° and 138° (parallel and perpendicular to the ENLR direction, respectively) at several different offsets from the nucleus. Different slit widths were used, from 0″.22 to 0″.65. The slit positions are shown in Figure 1, and the log of the observations is given in Table 1.

The individual frames were reduced using the FIGARO image processing environment (Shortridge 1993) and then rebinned to a resolution of 0.24 Å pixel^{-1} (60 km s^{-1}). The continuum spectra were subtracted after correction for vignetting effects and the spatial distribution of emission-line fluxes, central velocity, and FWHM obtained by fitting Gaussian functions to the line profiles using the LONGSLIT spectral analysis software (Wilkins & Axon 1992).

2.2. *HST FOC f/48 Data*

The NLR of NGC 4151 was observed using the *HST* Faint Object Camera (FOC) f/48 long-slit spectrograph on 1996 July 3. The slit, 0″.063 × 13″.5 in size, was positioned along PA = 47°. The F305LP filter was used to isolate the first-order spectrum that covers the 3650–5470 Å interval at a 1.58 Å pixel^{-1} resolution. The spatial scale is 0″.0287 pixel^{-1}, and the instrumental PSF is of the order of 0″.08. The observational procedure consisted in obtaining first an interactive acquisition (IntAq) image in the 1024 × 512 zoomed mode with the f/48 camera through the

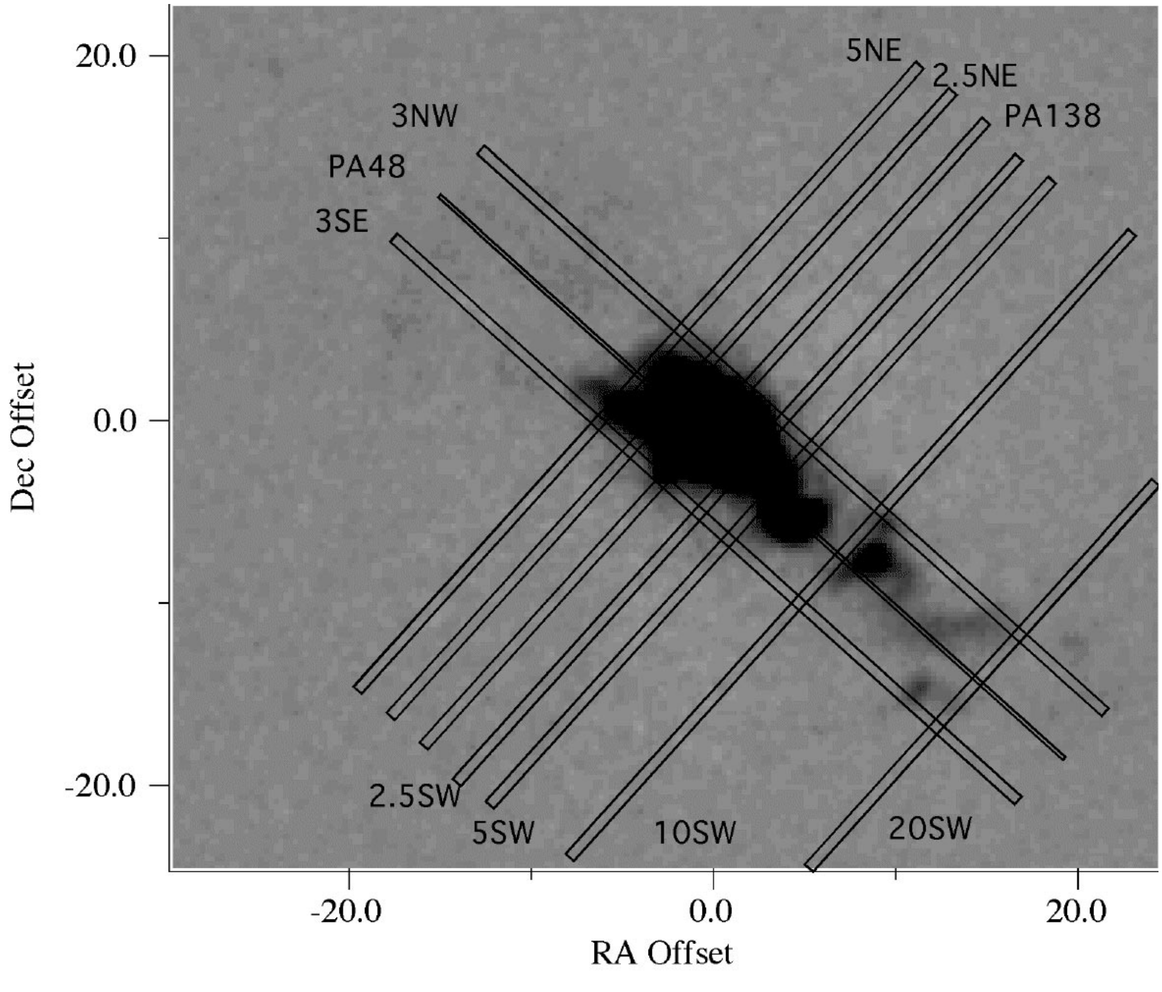

FIG. 1.—Slit positions of the ground-based spectra of Table 1 overlaid on the [O III] λ5007 image of the ENLR of NGC 4151 from Pérez et al. (1989)

TABLE 1

JOURNAL OF OBSERVATIONS: GROUND-BASED DATA

Name	PA (deg)	Offset from Nucleus (arcsec)	Exposure Time (s)	Slit Width (arcsec)	Seeing (arcsec)
5 NE.........	138	5 NE	1000	0.6	2.7
2.5 NE.......		2.5 NE	510	0.65	1.7
PA138		Nucleus	1050	0.62	2.2
2.5 SW[a]......		2.5 SW	500	0.65	1.7
5 SW		5 SW	1000	0.6	2.7
10 SW		10 SW	1000		
20 SW		20 SW	1000		
3 NW........	48	3 NW	1000		
PA48		Nucleus	1000	0.22	2.6
3 SE		3 SE	1000	0.6	2.7

[a] Spectrum obtained with a 0.6 neutral density filter.

F220W + F275W filters to allow for an accurate centering of the object. While the necessary offsets were calculated, a 1247 s, 1024 × 512 non–zoomed-mode spectrum was taken with the slit at the IntAq position. Six 697 s (nonzoomed) spectra were then obtained stepping across the NLR in 0″.2 intervals, starting 0″.6 southeast of the nucleus. The three resulting southeast spectra were too faint to be useful. The slit positions, derived as described below, are shown in Figure 2, superimposed on an archival [O III] λ5007 FOC f/96 image of the galaxy and listed in Table 2.

The spatial relation between objects in the sky is not preserved in the uncalibrated data from the cameras since the raw FOC images are affected by strong geometric distortion. This distortion comprises two components: the external or optical, due to the off-axis position of the detector itself, and the internal, a combination of the distortion caused by the magnetic focusing of the image intensifiers and the one introduced by the spectrographic mirror and grating. The internal contribution is by far the most important, and it is strongly time and format dependent. We have used both standard IRAF[6] procedures for spectroscopic data reduction as well as specific packages developed for the FOC data[7] to calibrate the data.

Initially, all frames, including those used for subsequent calibration, were geometrically corrected for the optical plus focusing-induced distortions using the equally spaced grid of reseaux marks etched onto the first photocathode in the intensifier tube. The observed positions of the reseaux

TABLE 2

JOURNAL OF OBSERVATIONS: *HST* DATA

Name	Data Set	Date	Exposure Time (s)	Format	Comments
Science Data					
NGC 4151......	X2PJ010CP	1995 Jul 11	934	1024 × 256	PA40_1 0″.57 SE
	X2PJ010DT		934	1024 × 256	PA40_2 0″.14 SE
	X2PJ010IT		598	1024 × 256	PA40_3 0″.14 NW
	X2PJ010JT		598	1024 × 256	PA40_4 0″.43 NW
	X2PJ010KT		598	1024 × 256	PA40_5 0″.52 NW
NGC 4151......	X38I0108T	1996 Jul 03	697	1024 × 512	PA47_1 Nucleus
	X38I0109T		697	1024 × 512	PA47_2 0″.23 NW
	X38I0102T		1247	1024 × 512	PA47_3 0″.41 NW
	X38I010AT		697	1024 × 512	PA47_4 0″.46 NW
Calibration Frames					
NGC 4151......	X2PJ010GT	1995 Jul 11	600	1024 × 512*z*	Internal flat
	X38I0106T	1996 Jul 03	600	1024 × 512	Internal flat
NGC 6543......	X3BD0102T	1996 Sep 10	682	1024 × 512	Planetary nebula
	X3BD0103T		717	1024 × 256	Planetary nebula
	X3BD0104T		600	1024 × 512*z*	Internal flat
	X3BD0105T		500	1024 × 512	Internal flat
47 Tuc	X34I0108T	1996 Apr 04	477	1024 × 256*z*	Globular cluster
	X34I0109T		600	1024 × 256*z*	Internal flat
LDS 749b	X3L8020BT	1996 Dec 27	497	1024 × 512	Flux standard
	X3L8020AT		800	1024 × 512	Internal flat

---

[6] IRAF is distributed by the National Optical Astronomy Observatories, which are operated by the Association of Universities for Research in Astronomy, Inc., under cooperative agreement with the National Science Foundation.

[7] Available at stsdas.hst_calib.foc.

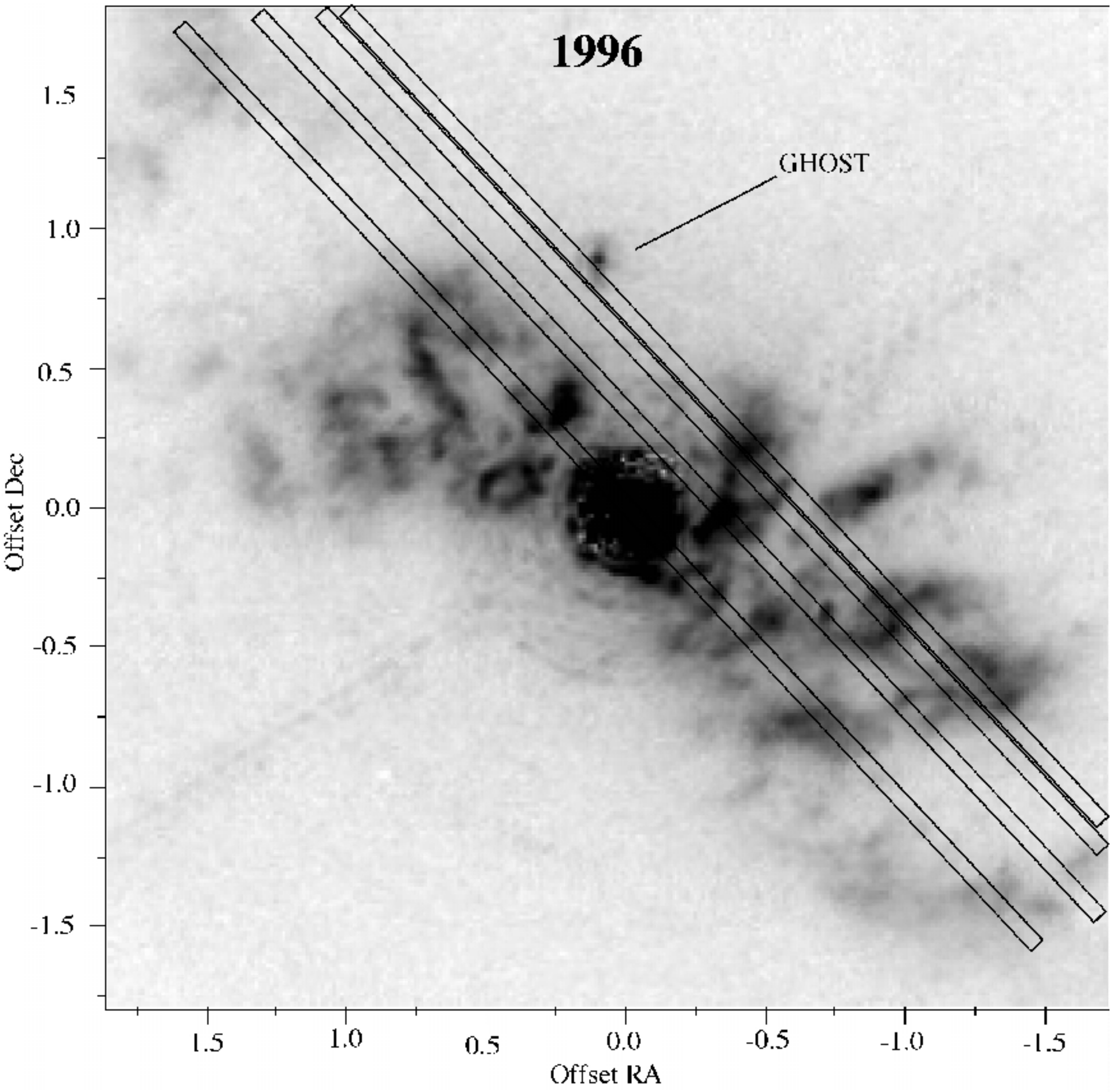

FIG. 2.—[O III] FOC f/96 image showing the position of the spectrograph slit for the 1996 spectra. The actual length of the slit is longer than represented. North is at the top, and east is to the left.

marks were measured in the internal flat-field frames bracketing the observations and then compared with an equally spaced artificial grid of suitable size (9 × 17 reseaux marks for the 1024 × 512 mode) already corrected by the *inverse* optical distortion.[8] Each individual transformation was computed fitting two dimensional Chebyshev polynomials of sixth order in x and y and fifth order in the cross-terms and applied to the respective science and calibration frames. The rms uncertainties in the reseaux positions are 0.12–0.20 pixel for the 512 mode, depending on the signal-to-noise (S/N) ratio of the flat-field images.

The remaining (mirror + grating) internal distortion along the dispersion direction was corrected by tracing the spectra of two stars observed in the core of the globular cluster 47 Tuc. The stars are ~130 pixels apart and provide a good correction for most of the working area of the slit. The rms of the tracing is about 0.2 pixel. The distortion along the spatial direction was obtained in a similar way, tracing the brightness distribution of the emission lines of the planetary nebula NGC 6543, with residuals of 0.10–0.22 pixel. The two corrections were combined in a single calibration file and applied simultaneously to the science frames.

Since the FOC spectrograph does not contain an internal reference source, the NGC 6543 geometrically corrected frame was used to obtain the wavelength calibration. Reference wavelengths were derived from ground-based observations (Pérez et al. 1999), which also indicate that distortions introduced by the internal velocity field of the nebula are negligible at the f/48 resolution (less than 0.5 Å ~ 0.3 pixel). The two-dimensional spectrum was collapsed along the slit, and a sixth-order Legendre polynomial solution found for the pixel-to-wavelength transformation, with residuals of ~0.04 Å. The lines were reidentified in the original frame and a bidimensional

---

[8] Determined from ray-tracing models of the *HST* and FOC optics and available within IRAF.

wavelength calibration file obtained. The spatially extended emission lines in the fully calibrated frame of NGC 6543 are measured to be within 0.13 Å of their reference values.

The procedure above can be summarized as follows:

1. Optical plus main geometric distortions are corrected using the reseaux marks and leave a residual error of 0.12–0.20 pixel.
2. Residual (spectrograph) distortion in the dispersion direction is corrected tracing the spectra of point sources, and the error is ~0.2 pixel.
3. Residual distortion along the slit is corrected tracing the emission lines of an extended source, and the error is 0.10–0.22 pixel.
4. Errors from internal velocity field of the wavelength calibrator and from the calibration itself are less than 0.5 and 0.13 Å, respectively.

The final errors estimated for the NGC 4151 spectra, combining all the above sources in quadrature (including the errors from the geometric corrections applied to the calibration files), are 0″.016 and 1.1 Å rms in the spatial and dispersion directions, respectively. The final wavelength resolution is ~310 km s^{-1} at [O III] λ5007.

Flux calibration was obtained using the UV standard star LDS 749b. The data frame was geometrically corrected and wavelength calibrated as above, and the spectrum extracted on a 16 pixel window. This was then divided by the integration time and by the appropriate segment of the absolute flux table, rebinned to match the wavelength interval. A sixth-order spline3[9] was fitted to the resulting counts per flux per second spectrum, averaged in 60 Å intervals, generating a smooth response function. The vignetting along the spatial direction was corrected using the model presented in the FOC Handbook (Nota et al. 1996) and combined with the above response function to obtain a two-dimensional sensitivity calibration frame. We estimate light losses due to the small size of the slit to be in the order of 20% for a point source. The relative flux of lines measured within a 0″.3–0″.6 (10–20 pixels) interval is believed to be accurate at a 10%–15% level.

The science frames were divided by the exposure time and by the composite sensitivity frame. The background emission was subtracted by fitting a spline3 function along both spatial and dispersion directions, after masking the regions with emission lines and continuum. We opted to keep the fitting function order as low as possible, which provides the best subtraction over most of the frame, even when this implied an imperfect result over small areas, where the background was larger and/or a more rapidly varying function of position. An example of the resulting two-dimensional frames is shown in Figure 3. The plots correspond to a 2″.6 × 71 Å (166 pc × 4250 km s^{-1}) segment of the [O III] λ5007 emission line centered on the nuclear continuum on the PA47_1 spectrum (*top*) and 0″.6 southwest from the center of the slit on the PA47_3 spectrum (*bottom*). Multiple velocity systems and a complex cloud structure are seen, and some features can be easily identified in the spectra shown in Figure 7, like the broad plume 0″.37 southwest of the nucleus in the top image or the double-peaked feature and high-velocity cloud 0″.2 and 1″ southwest, respectively, in the 0″.41 northwest image.

To determine the slit positions accurately, we compared the [O III] λ5007 luminosity profile of each spectrum with that derived from an archive FOC f/96 image taken with the F501N filter. The observed spectra were convolved with the

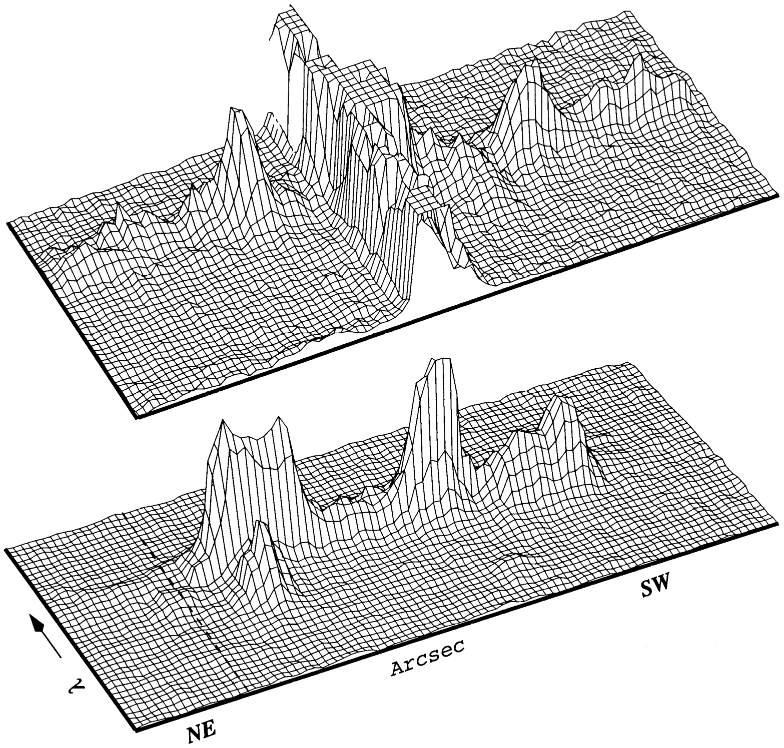

FIG. 3.—Surface plots of a segment of the nuclear (PA47_1, *top*) and 0″.41 NW (PA47_3, *bottom*) FOC f/48 1996 spectra in the [O III] λ5007 region. Both regions are 2″.6 by 71 Å (166 pc by 4250 km s^{-1}).

---

[9] The "order" of a liner or cubic spline function in the IRAF routines refers to the number of polynomial pieces in the sample region.

transmission curve of the filter and the data collapsed along the dispersion direction. The f/96 image was rebinned to match the f/48 spatial resolution and the spectra light profiles compared with the sum of two successive lines stepping across the image at PA = 47°. The final agreement is good within a few percent, and the final uncertainty in the position corresponds to half the size of the slit (or one line in the image), 0″.03.

We also retrieved from the *HST* Archive the NGC 4151 spectra obtained on 1995 July 11 as an engineering test of the f/48 detector. The slit was positioned at PA = 40°, and the spectra were taken using the 1024 × 256 mode. Data reduction was complicated by the lack of an equivalent flat-field frame (the ones interspersed with the observations were taken in the 1024 × 512 zoomed mode) and contemporaneous wavelength calibration observations, resulting in larger uncertainties in both spatial and spectral scales. Owing to the higher background features located in the upper and middle part of the frames, as well as the presence of a serious "blemish" in the detector crossing over part of the [O III] λλ4959, 5007 emission lines, we have chosen to optimize the reduction for the [O II] λ3727 region, which results in final uncertainties of 0″.02 and 1.24 Å in the spatial and dispersion directions, respectively. We note, however, that several emission and kinematic features observed in the 1996 [O III] data can also be identified in the 1995 frames (see § 3). Five data sets contain enough signal to be useful, and their positions, derived in a similar way to the 1996 data, are listed in Table 2 and shown in Figure 4.

3. RESULTS

3.1. *Ground-based Data*

Figure 5 shows a selection of the [O III] λ5007 line profiles observed along the PA48 position at various offsets from the nucleus. In the inner 5″ (the NLR), up to three Gaussian components were needed to fit the line profiles, while the extended emission was well represented by a single Gaussian with the instrumental resolution (~45 km s^{-1}). The transition between the ENLR and the inner NLR at around 4″ is particularly instructive. Here, the extended narrow component is joined by a second blueshifted component of ~400 km s^{-1} FWHM. Interior to this radius, the line profiles are always broad and double.

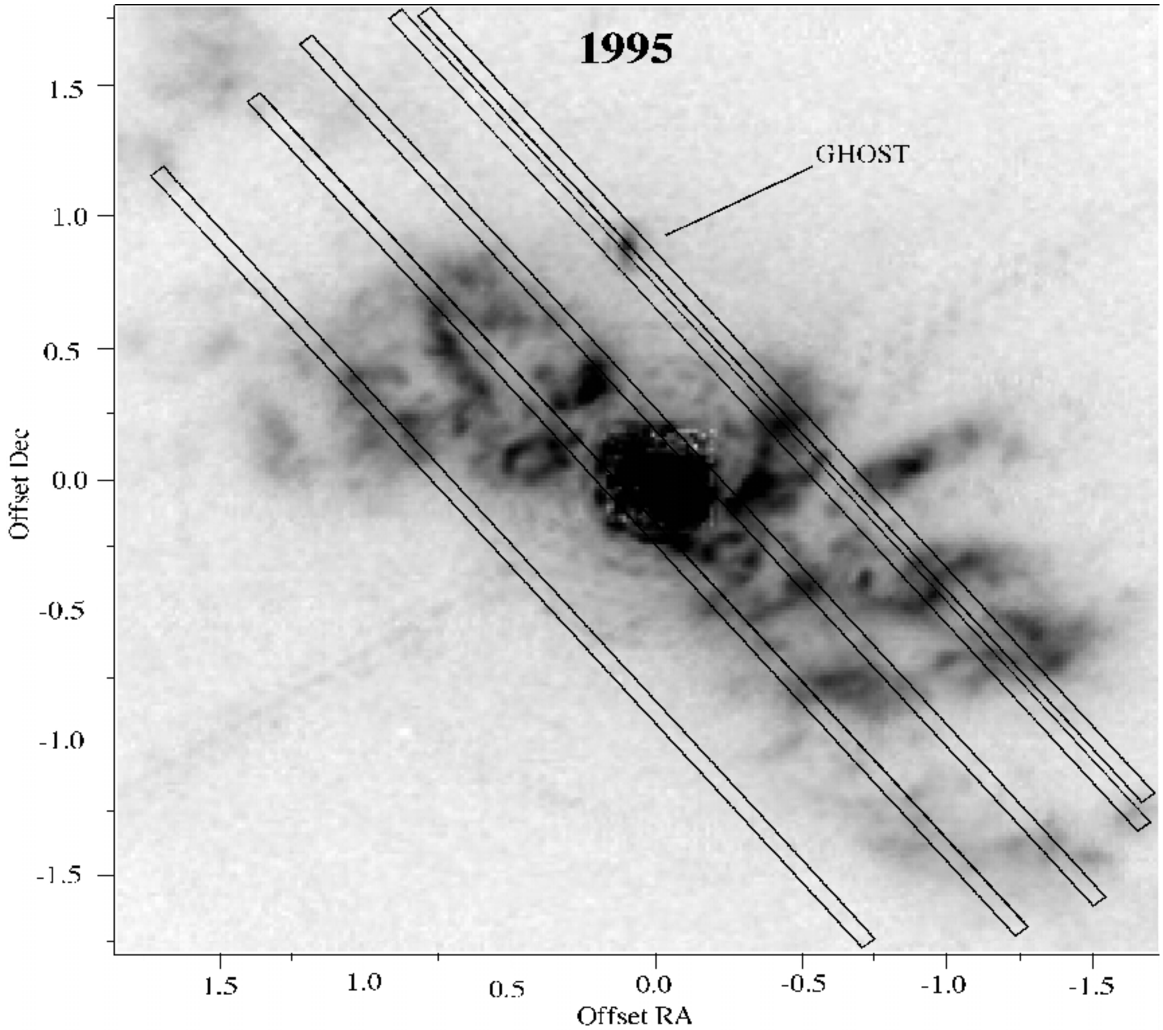

FIG. 4.—[O III] FOC f/96 image showing the position of the spectrograph slit for the 1995 spectra. Orientation as in Fig. 2.

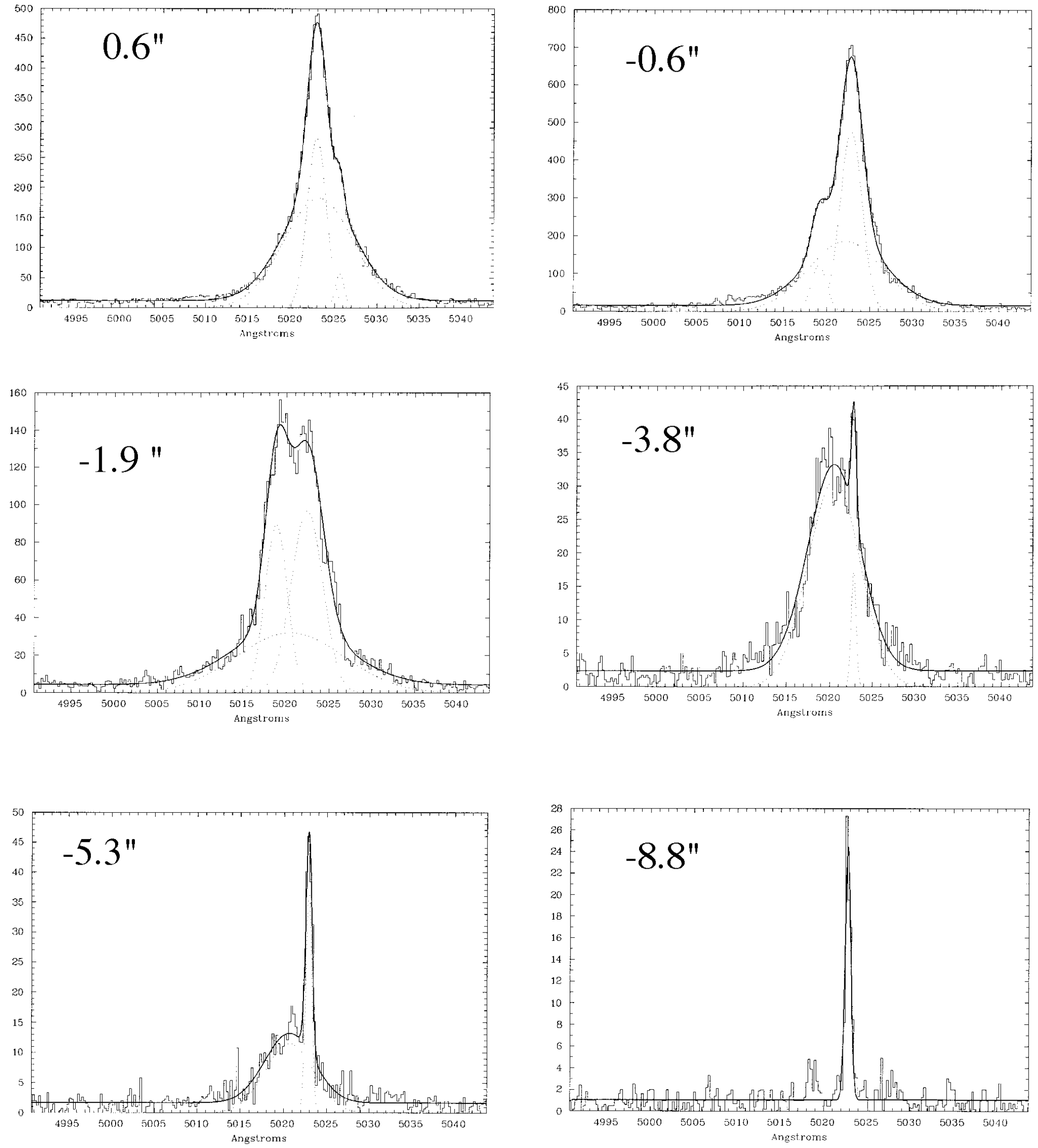

FIG. 5.—Sample of INT [O III] λ5007 line profiles and Gaussian fitting. From top left to bottom right: 0″.6 northwest of the nucleus; 0″.6 southwest; 1″.9 southwest; 3″.8 southwest; 5″.3 southwest; and 8″.8 southwest. Notice how the narrow extended component can be traced into the inner 5″ of the NLR.

Figure 6 presents the result of the profile analysis for the PA48 position. It can be seen that the velocity structure of the extended emission (shown as stars) is similar to that of a typical galactic rotation curve, which indicates that this emission originates from gas in the galactic plane. The line width of <45 km s^{-1} is also consistent with the velocity dispersion of gas in the disks of normal spiral galaxies (van der Kruit & Shostak 1984). This component has a ratio [O III]/Hβ ~ 9, indicating it is photoionized by the AGN continuum. The general impression is that the FWHM of this primary component increases steadily as one approaches the nucleus, while the radial velocity connects almost seamlessly onto the velocity field of the extended narrow component, a point we shall reemphasize when we discuss the FOC f/48 results. This progression is well illustrated by the line profiles between 1″.9 and 3″.8 southwest (Fig. 5, *middle panels*). The second component (*open squares*) is much broader, FWHM $\sim$ 600 km s^{-1}, is present only in the inner 5″ of the emission region, and is systematically blueshifted with respect to the primary. The [O III]/Hβ ratio is ~ 7. At first sight, the physical reality of the third, narrower, component (FWHM $\sim$ 100 km s^{-1}), which is found only very close to the nucleus, with high velocity shifts with respect to the main rotation curve, may be thought to be questionable. However, as we shall see, it corresponds to structures identified in the high spatial resolution FOC f/48 data, closely associated with the radio jet.

3.2. *HST FOC f/48 Data*

To study the kinematics of the gas in the *HST* spectra, the brightest emission lines, [O II] λ3727 and [O III] λλ4959, 5007, were extracted in spatial windows varying from 2 to 20 pixels along the slit and their profiles fitted using one to three Gaussian components. The two [O III] lines were fitted simultaneously, constraining the physical parameters of the corresponding components of each line to their theoretical values (3:1 intensity ratio, 48 Å separation, and the same FWHM). Figure 7 shows some examples of the fits for the 1996 [O III] region. The spectra are identified by their distance to the center of the slit, defined as the line passing

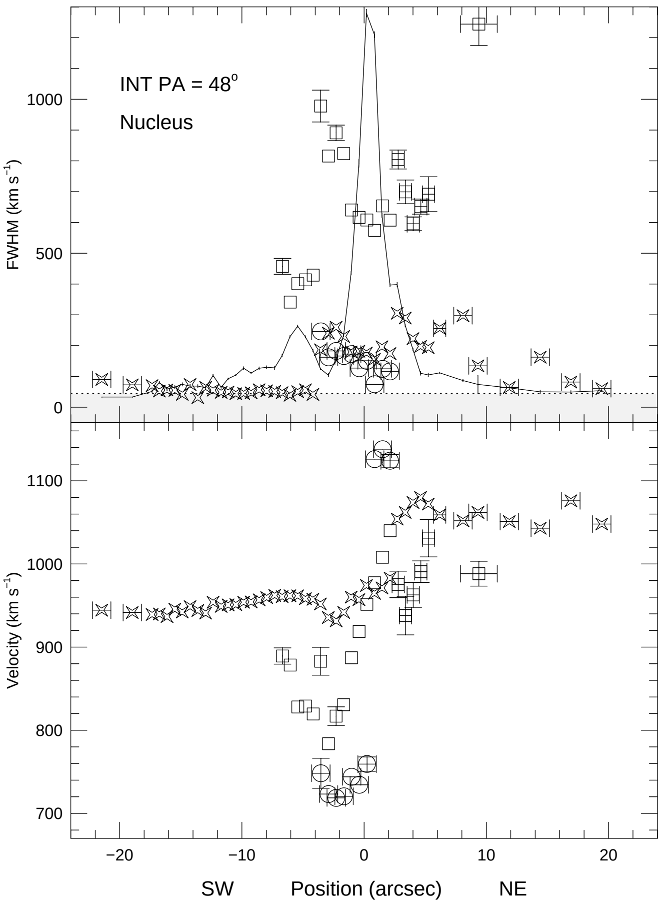

FIG. 6.—Result of the Gaussian decomposition procedure for the [O III] $\lambda 5007$ line of the INT PA48 spectrum. The velocities derived from the central wavelength of the individual components are shown in the bottom panel. The top panel presents the corresponding FWHM, and the solid line is the brightness profile of the narrow component. The data are plotted as a function of the distance to the center of the slit. For this and the other similar figures in the paper, error bars smaller than the point size are not plotted. *Stars*: main narrow component; *squares*: broad component; *open circles*: high-velocity narrow component.

through the nucleus perpendicular to the slit direction, with negative values running toward the southwest. All regions plotted are located within 1″.5 from the active nucleus, and the line profile representations vary from a single component, with very little broadening (second spectrum at position PA47_3), to combinations of very broad or multiple Gaussians.

Figure 8 shows two regions of the [O III] $\lambda\lambda 4959$, 5007 emission in the 1995 0″.14 and 0″.52 northwest (PA40_3 and PA40_5) frames, which correspond to the same kinematical features already remarked in Figure 3, the nuclear plume and the double-peaked profile. Even with the presence of the blemish redward of [O III] $\lambda 5007$, the similarity with the nearby 1996 profiles is evident.

The results of the decomposition are shown in Figures 9*a*–9*d* for the 1996 [O III] $\lambda 5007$ data, where the top panels show the FWHM of the different components superimposed over the brightness profiles of the radio emission (from the VLA + Merlin 5 GHz radio map of Pedlar et al. 1993). In these figures, the data are plotted as a function of position along the slit. The resulting components naturally separate into three groups: a narrow (FWHM $\lesssim$ 700 km s^{-1}) one, closest to the systemic velocity and usually the brightest component in the fit (*filled triangles*); a broad (FWHM $\gtrsim$ 700 km s^{-1}) base that appears in the highest S/N spectra and is distributed around the radio knots (*stars*); and the occasional narrow secondary component, which can be split from the main emission by as much as ±1000 km s^{-1} (*open circles*). The gray region is the instrumental FWHM. The seven points on the PA47_1 (nuclear) position plotted as open triangles will be discussed later (see § 4.2.2).

As discussed in Paper I, there is an association between the optical and the radio emission, in the sense that the brightest emission-line filaments surround the radio knots, as expected in a scenario in which the plasma of the radio jet is clearing a channel in the surrounding medium and enhancing the line emission along its edges by compression of the ambient gas (Taylor, Dyson, & Axon 1992; Steffen et al. 1997a, 1997b). Figures 9*a*–9*d* present the kinematic expression of this association, with broad bases and/or high-velocity components closely associated with the radio emission, while the "main" narrow component follows a more ordered pattern, which strikingly resembles that of a disk rotation curve.

The lower resolution (instrumental FWHM ~ 450 km s^{-1}) and lower S/N in the [O II] $\lambda 3727$ region did not allow us to isolate as many components as for [O III] $\lambda 5007$. Nevertheless, the overall behavior of the velocity field, shown in Figures 10 and 11 for the 1996 and 1995 data, respectively, is the same as for the [O III] $\lambda 5007$ emission, with the narrow component tracing rotation in the disk, while the broad and secondary components mark the interaction of the radio plasma with the ambient gas.

Based on our observations, we propose that the emission gas in the inner 5″ of NGC 4151 is, to the first order, produced by the central source's photoionization of the ambient gas located in the disk of the galaxy, and therefore, its kinematic behavior is mainly planar rotation, determined by the dominant potential in the nuclear region (either a very concentrated but extended mass distribution or a central massive dark object). The ionizing photons escape along a broad cone that grazes the disk, as suggested by Pedlar et al. (1992), and Robinson et al. (1994). From our data we can see that the systematic outflow previously remarked on the literature (see, e.g., Schulz 1990) as dominating the kinematics of the emission gas in the NLR of NGC 4151 can be understood as an effect of the lack of spatial resolution of the ground-based data. When the spectra of the individual clouds are obtained, it is possible to decouple the gas that is in general rotation in the disk under the gravitational influence of the central mass concentration from that which is being entrained and swept along by the radio plasma, as it plunges through the galactic disk. This scenario has already been suggested by Vila-Vilaró et al. (1995), based on a higher (0.34 arcsec pixel^{-1} and ~1″ seeing) spatial resolution ground-based spectrum oriented along PA = 51°, where they found that the emission within 3″ from the active nucleus can be decomposed into one blueshifted component located mainly southwest of the nucleus, and a second system that they describe as appearing "to link the blueshifted ENLR SW of the nucleus with the redshifted emission to the NE. It is conceivable that it represents a continuation of the ENLR velocity field and hence traces the galactic rotation curve within the NLR." Mediavilla et al. (1992) also remarked on the existence of a gradual connection between the kinematic and

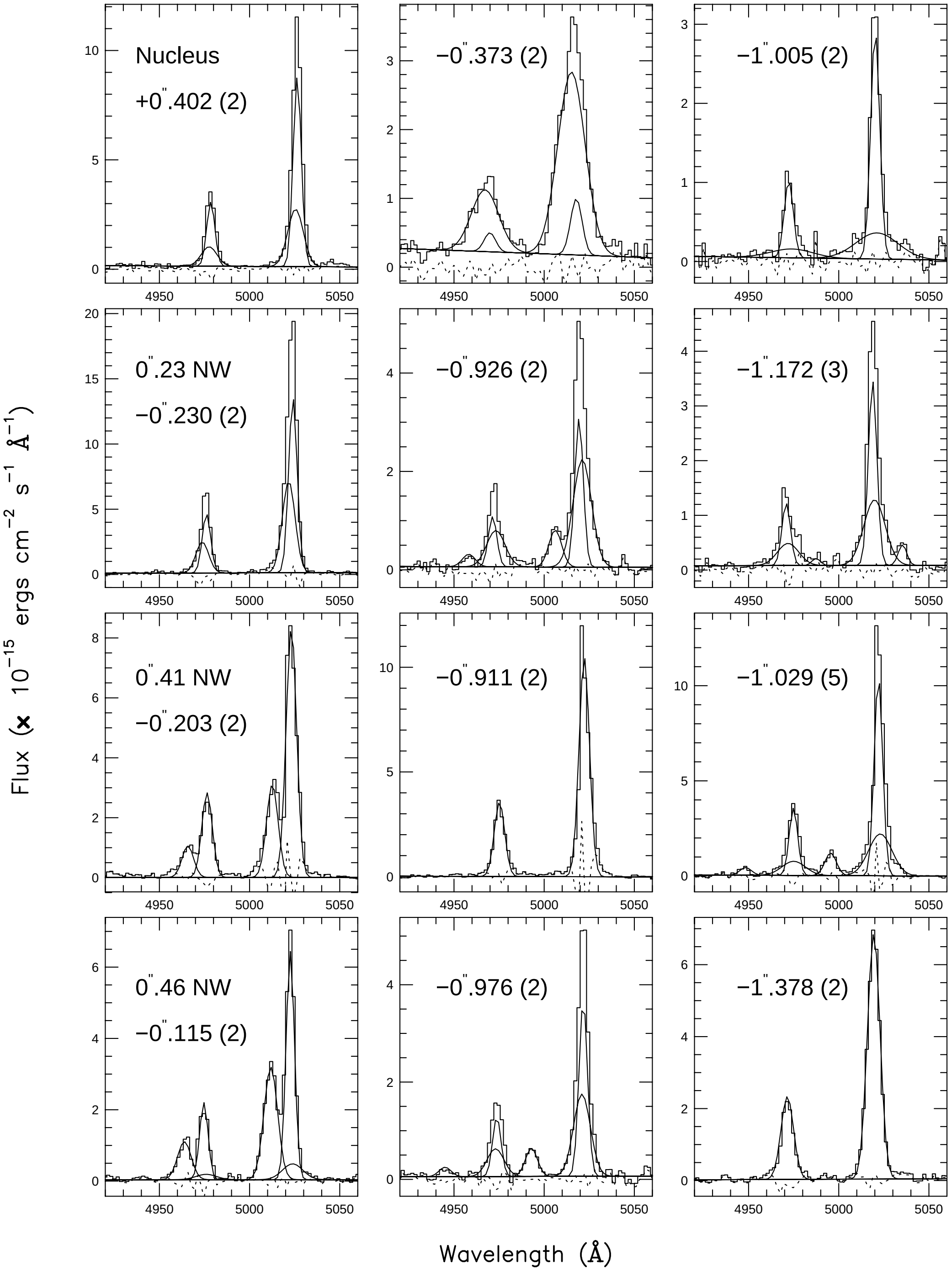

FIG. 7.—Gaussian fitting to a sample of [O III] λλ4959, 5007 line profiles from the FOC f/48 1996 spectra. The spectra are identified by their distance in arcseconds to the center of the corresponding slit, negative values to the southwest. The number after the distance corresponds to how many columns in the image were co-added. The histogram is the data, the thin lines represent the individual components and underlying continuum, and the dotted line represents the residuals of the fit.

physical properties of the galactic environment and the (ground-based) unresolved inner NLR.

We also note that if the scenario of an outflow along the edges of the ionization cone is invoked, it is necessary for the line of sight to be located outside the cone or systematic blueshifted components would be projected on both the southwest and northeast sides, which is not observed. A narrow cone, however, implies a ∼25° misalignment between the outer ENLR and the direction of the radio jet and therefore to a geometry that is distinct from the "standard" unified model. Pedlar et al. (1993) first remarked on the presence of small, systematic changes in the jet orientation, since the position angle of the jet in the inner 3″ southwest oscillates between 254° and 263° (74°–83°), with an approximate mirror symmetry to the northeast side. The abrupt change of 55° in the direction of the radio emission in the milliarcsecond scale as seen in the VLBA radio maps of Ulvestad et al. (1998) suggests that effects such as precession or warping are very likely present in the collimating structure around the central source

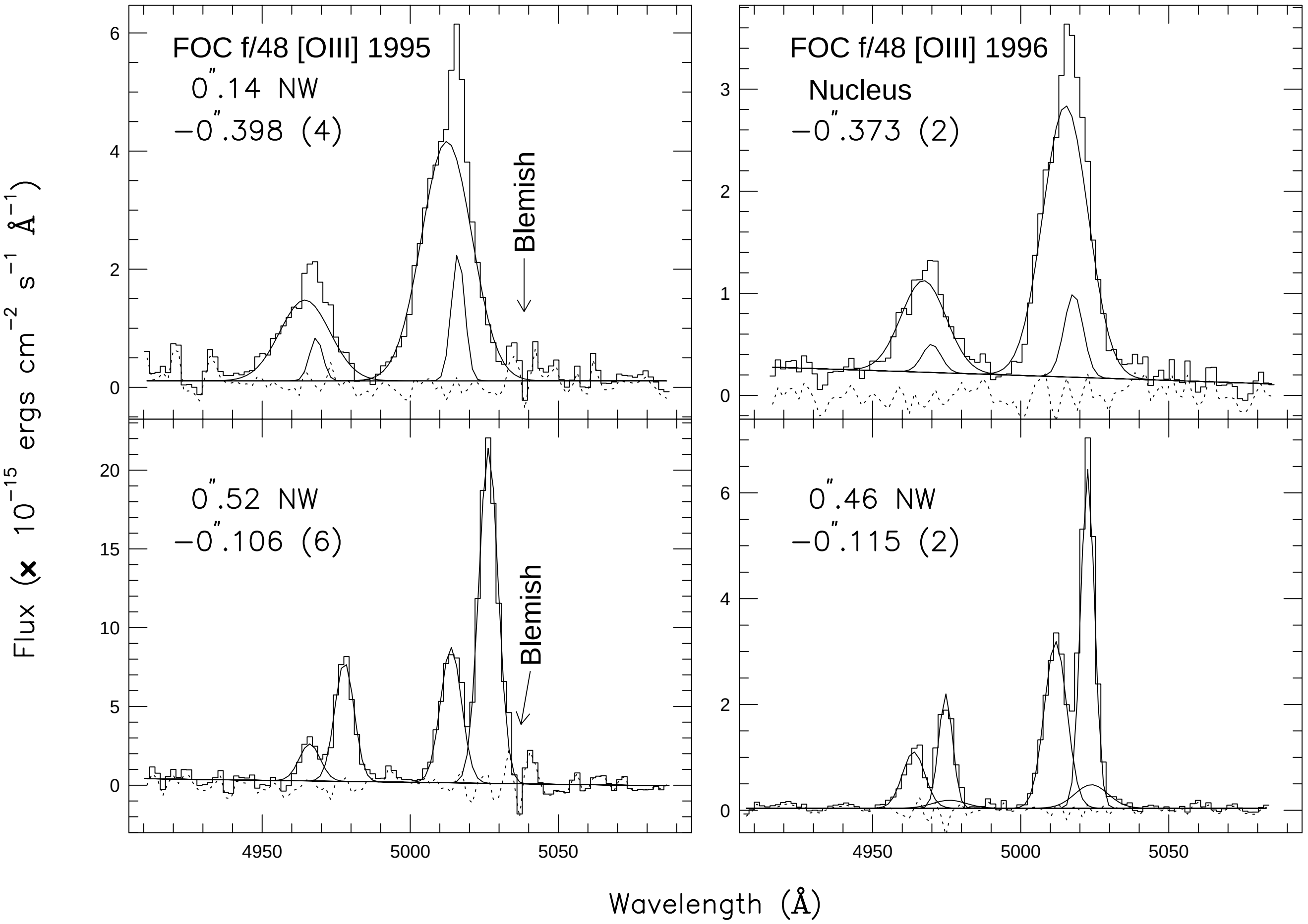

FIG. 8.—Same as Fig. 7 for two positions on the 1995 FOC f/48 spectra (*left*) and the regions closest to them in the 1996 data (*right*)

(Pringle 1997), but the fact that the arcsecond-scale radio jet is aligned within 10° indicates that these effects would be transient and their impact in the alignment and morphology of the NLR/ENLR/radio emission are difficult to determine.

The presence of the variable blueshifted optical and UV absorption lines is clear evidence that a gas outflow *is* present in the nuclear region of NGC 4151. The high-resolution GHRS spectra presented by Weymann et al. (1997) show the existence of several distinct systems with outflow velocities from 300 to 1600 km s^{-1} with respect to the nucleus, but the material responsible for these features is very likely to be located inside 1 pc of the active nucleus, and the actual geometry and dynamics of the clouds is not known (Espey et al. 1998). Although tempting, to associate the bulk kinematics of the emission-line gas of the NLR on scales of several to hundreds of parsecs with the nuclear outflowing gas is not consistent with our data, since we observe very localized clouds with both blue- *and* redshifted emission within the velocity range quoted for the outflows above, while the bulk of the gas can be well described by a planar rotation model.

4. MODELING THE ROTATION CURVE

To study the gas velocity field, we concentrate on the narrowest, closer to the systemic velocity, and most frequently the brightest, Gaussian component (Figs. 9–11, *filled triangles*) as representative of the "main" NLR emission. The same argument was used to define the ground-based rotation curve (see § 3.1). In the ENLR, the general behavior of the velocity field connects smoothly with that of the neutral gas in the kiloparsec scale (see, e.g., Vila-Vilaró et al. 1995). Here, we proceed on the assumption that the gas represented by the "main" component of the velocity field we isolated in the *HST* data is, to a first approximation, also participating in the general rotation of the gas in the galactic disk, since it also connects reasonably well with the extended emission, as can be seen in Figure 12.

4.1. *The Model*

We have used the Bertola et al. (1991) analytic expression, which provides a simple parametric representation for particles (gas or stars) on circular orbits in a plane, in the form

$$V_c(r) = V_{\rm sys} + \frac{Ar}{(r^2 + C_0^2)^{p/2}}\,, \qquad (1)$$

where $V_{\rm sys}$ is the systemic velocity, r is the radius in the plane of the disk, and A, C_0, and p are parameters that define the amplitude and shape of the curve. If $v(R, \Psi)$ is the radial velocity at a position (R, Ψ) in the plane of the sky, where R is the projected radial distance from the nucleus and Ψ its corresponding position angle, we have

$$v_{\rm mod}(R, \Psi) = V_{\rm sys} + \frac{AR \cos(\Psi - \Psi_0) \sin i \cos^p i}{\{R^2\eta + C_0^2 \cos^2 i\}^{p/2}}\,, \qquad (2)$$

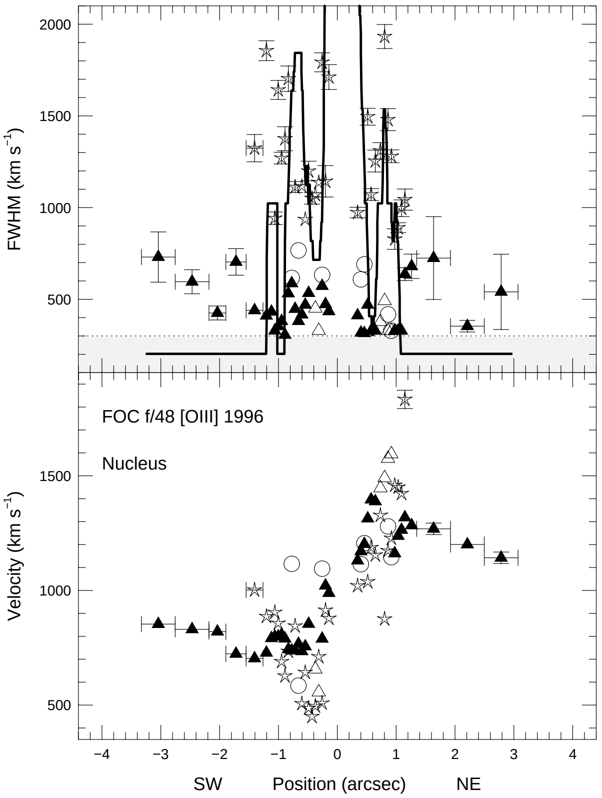

FIG. 9*a*

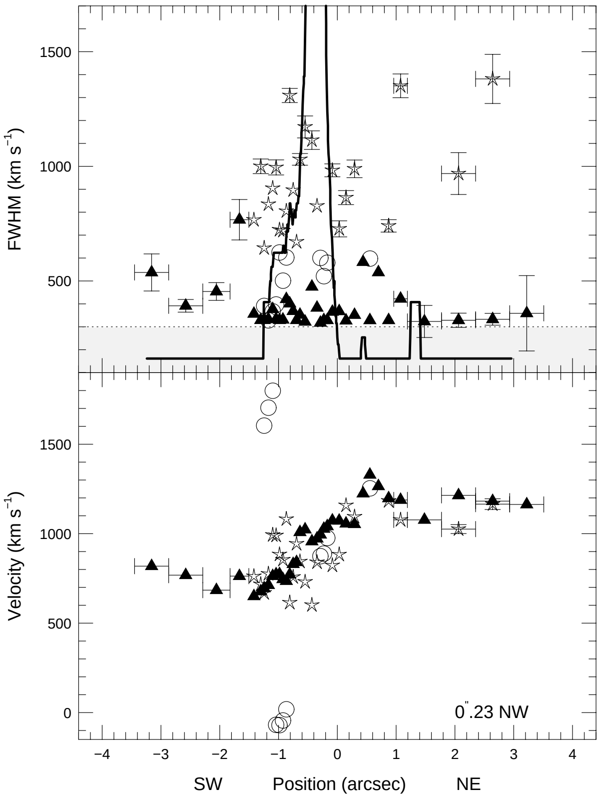

FIG. 9*b*

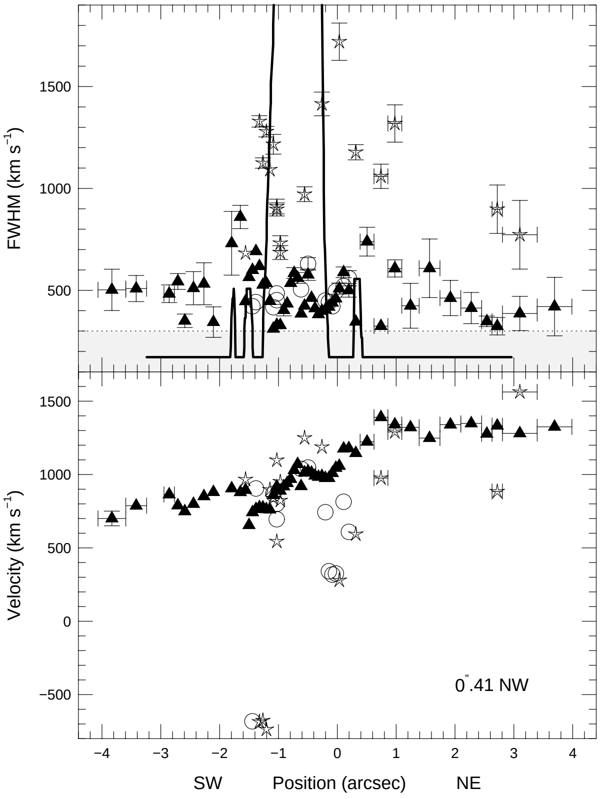

FIG. 9*c*

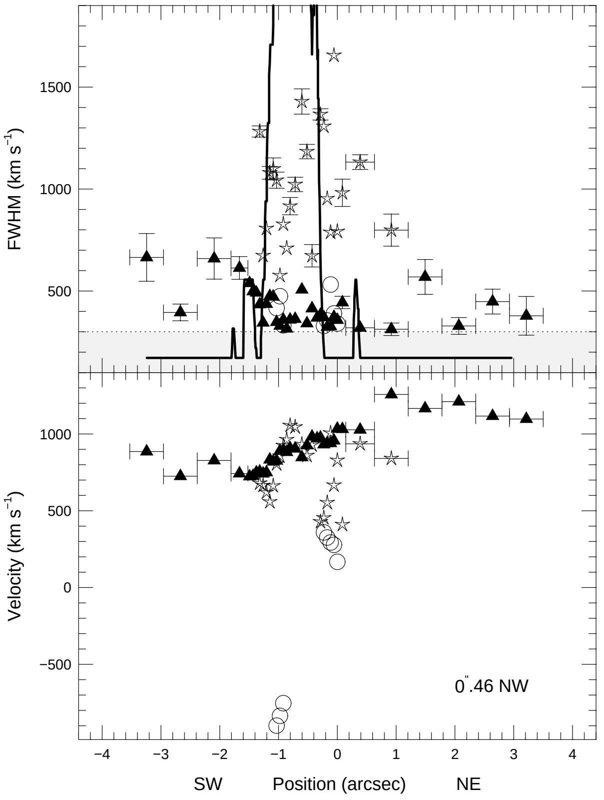

FIG. 9*d*

FIG. 9.—Result of the Gaussian decomposition procedure for the [O III] λ5007 line of the 1996 FOC f/48 spectra: (*a*) Nucleus, (*b*) 0".23 northwest, (*c*) 0".41 northwest, and (*d*) 0".46 northwest. The velocities derived from the central wavelength of the individual components are shown in the bottom panels. The top panels present the corresponding FWHM superposed to the VLA + Merlin 5 GHz brightness profile at each slit position. Both are plotted as a function of the distance to the center of the slit. *Filled triangles*: main narrow component; *open circles*: narrow secondary component; *stars*: broad component.

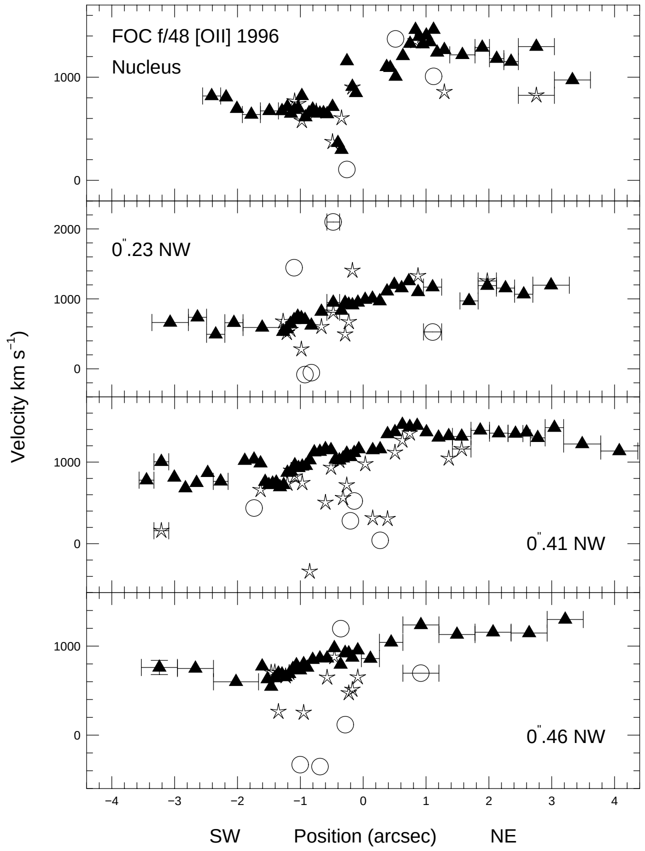

FIG. 10.—Rotation curves derived from the Gaussian decomposition of the 1996 FOC f/48 [O II] λ3727 line. From top to bottom: Nucleus, 0".23 northwest, 0".41 northwest, and 0".46 northwest. Symbols as in Fig. 9.

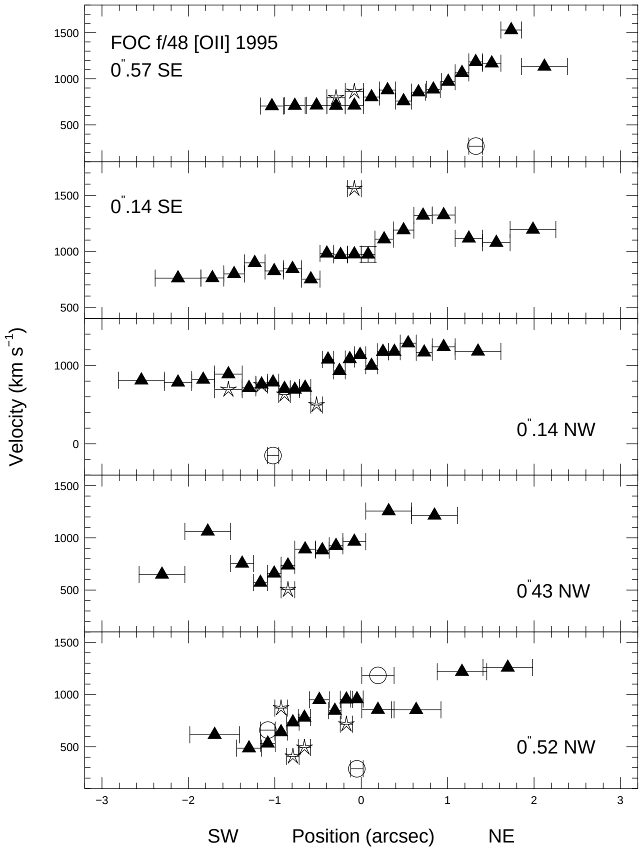

FIG. 11.—Same as in Fig. 10 for the 1995 FOC f/48 [O II] λ3727 line. From top to bottom: 0".57 southeast; 0".14 southeast; 0".14 northwest; 0".43 northwest; 0".52 northwest. Symbols as in Fig. 9.

where

$$\eta \equiv [\sin^2 (\Psi - \Psi_0) + \cos^2 i \cos^2 (\Psi - \Psi_0)] ,$$

where i is the inclination of the disk ($i = 0°$ for a face-on disk) and Ψ_0 is the position angle of the line of nodes.

4.2. *The Fitting*

We used a Levenberg-Marquardt nonlinear least-squares algorithm to fit the above model. The various parameters are determined simultaneously by minimizing the residuals $\Delta v = (v_{\rm obs} - v_{\rm mod})$, with $v_{\rm mod}(R, \Psi; A, C_0, p, i)$ and $v_{\rm obs}(R, \Psi)$ being the model and observed radial velocities at the position (R, Ψ) in the plane of the sky, respectively.

The rotation curve expressed in equation (2), while giving a simple representation of the gas kinematics, has a few shortcomings from the point of view of a minimization procedure. The two projection angles, i and Ψ_0, can be independently determined only if data are available for more than one position angle in the galaxy. In a single run of the program, they are also strongly dependent on the initial values provided to the algorithm.

The parameters A and i are strongly coupled when determining the amplitude of the rotation curve, so equally acceptable fits can be obtained with a large A and a small i or vice versa. This situation is more acute for $p \sim 1$, and the two parameters tend to decouple for larger values of the exponent. The parameter C_0 is determined mainly by the steepness of the inner part of the rotation curve, which implies that the use of off-nuclear slit positions will tend to push its value to larger radii simply by the absence of data corresponding to smaller values of R. On the other hand, the exponent p is determined by the outer parts of the rotation curve, and its value is expected to be between 1 for a "dark halo" potential and 1.5 for a system with finite mass contained within the "turnover" radius. Evidently, data

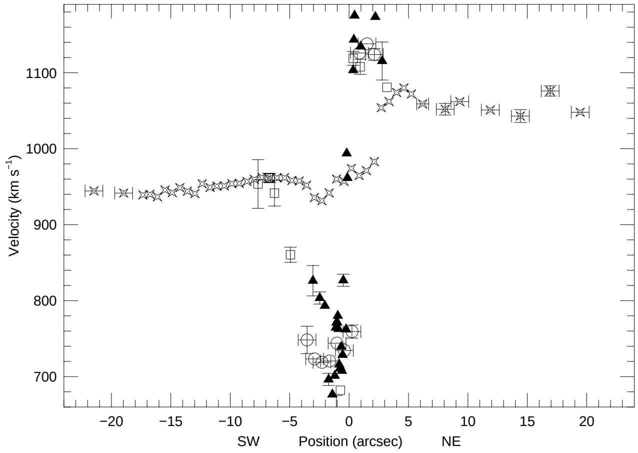

FIG. 12.—Comparison between the ground-based ENLR rotation curve (PA48 position; first component, *stars*; third component, *open circles*), with the FOC f/48 data (PA47_1; *filled triangles*) and the STIS slitless data from Hutchings et al. (1998) (*open squares*) corresponding to clouds closer to PA = 48°.

points for larger values of R will tend to reflect the potential generated by the mass distribution on larger scales.

To test the algorithm, we used the original data (with added errors of 5%–10%) from Bertola et al. (1991) on NGC 5077 and followed the same procedure described in their paper. Our resulting model agrees with theirs within an rms of 8 km s^{-1}, with the final parameters differing by less than 5%. Also, applying the algorithm to an artificial rotation curve with spatial sampling and added errors similar to those of the NGC 4151 data retrieves the original parameter set to better than 1%.

4.2.1. *The Ground-based Data Set*

To derive the projection angles of the galaxy's disk, we used the ground-based data listed in Table 1 and excluded from the fit the points within 5″ from the active nucleus since the spatial resolution does not allow us to separate the "main" rotating component from the highly disturbed gas interacting with the radio jet in the NLR.

Initially, the data from the three slit positions at PA = 48° were fitted with A, p, C_0, i, Ψ_0, and $V_{\rm sys}$ as free parameters, with $V_{\rm sys}$ having the same value for all data points. Then, to take into account any residual zero point velocity offsets between the data sets, each position angle was separately fitted, allowing $V_{\rm sys}$ to vary but keeping the remaining parameters fixed to the values obtained before. The resulting systemic velocity for each position was subtracted from the observed values and the whole data set refitted with now five free parameters. Once convergence was achieved, the new model was used to obtain the value of $V_{\rm sys}$ at each slit position, and the procedure repeated. The model was found to be stable at the third iteration, and the velocity offsets between data sets were smaller than 10 km s^{-1}.

Finally, the effect of the initial guess on the parameters was explored running the program for a wide interval of Monte Carlo search for each parameter, while the others were given the best-fit values as the initial guesses. The resulting ranges in the best-fit parameters are shown in Table 3. They tend to cluster in two families characterized by different values in the position angle of the line of nodes (Ψ_0). Since the least-squares minimization is unable to select between them, the two average models for these families are also listed as models A and B and are plotted in Figure 13. There we see that our data alone are not enough to allow us to discard either of these models, so we choose the value of Ψ_0 as 33°.9, which is closer to the results quoted in the literature ($\Psi_0 = 29°.1 \pm 2.4$ at $R = 10''$ from H I 21 cm observations—Pedlar et al. 1992; $\Psi_0 \sim 34°–41°$ at $R = 2''.5$ from Hα + [N II] measurements—Mediavilla & Arribas 1995). We stress that the final model obtained from the *HST* data is essentially insensitive to the exact choice of value within this narrow range, and therefore for simplicity, in the rest of this paper we present only the analysis carried out using model A.

TABLE 3

MODEL FITTING: GROUND-BASED[a]

Parameter	Range	Model A	Model B
A (km s^{-1})......	170–186	181	182
p	1.0	1.0	1.0
C_0 (arcsec)	6.4–7.4	7.1	6.6
Ψ_0 (deg).........	31–48	33.9	43.7
i (deg)	18–23	21.8	20.9

[a] PA = 48° data.

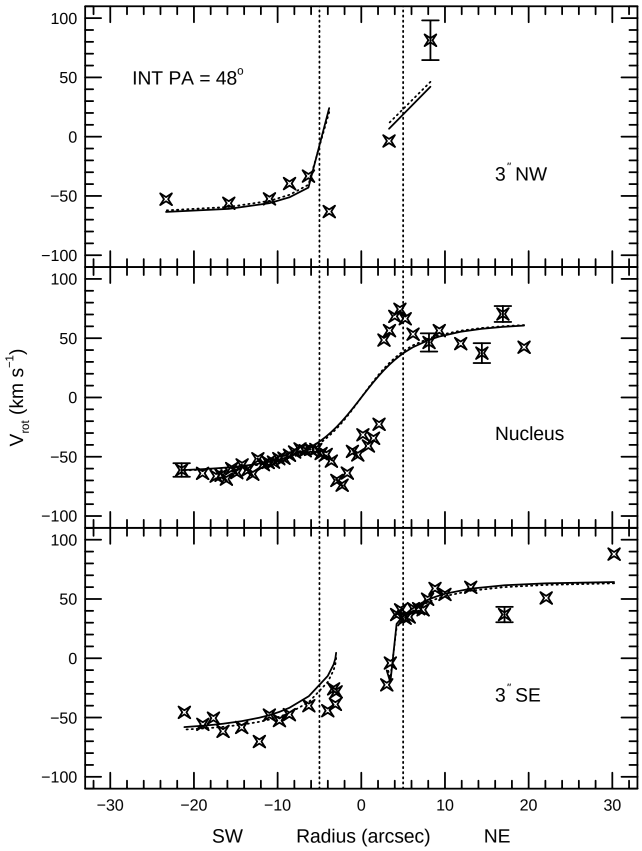

FIG. 13.—Comparison of the observed radial velocities from the INT (PA = 48°) data with the best fitting circular rotation curve from eq. (1), corresponding to models A (*solid line*) and B (*dotted line*) on Table 3. The vertical lines mark the region excluded from the fit owing to the interaction of the emission gas with the radio jet.

Other than that, the final solution is stable in all parameters: the inclination of the disk, $i = 21°$, agrees very well with other photometric and kinematic determinations (Simkin 1975; Bosma, Ekers, & Lequeux 1977; Pedlar et al. 1992); the rotation curve derived from the emission gas in the ENLR is essentially flat for $R \gtrsim 15''$ ($\sim$1 kpc), as observed from H I and optical data (Pedlar et al. 1992; Robinson et al. 1994; Vila-Vilaró et al. 1995; Asif et al. 1997); the amplitude A is typical of the values observed for normal galaxies with similar absolute magnitude and Hubble type (Rubin et al. 1985). On the other hand, the parameter $C_0 \sim 440$ pc, which for $p = 1$ is the radius at which the velocity reaches 70% of its maximum value, is smaller than the typical value of ≥ 1.0 kpc, which indicates a large central mass concentration.

Using the model A above to obtain the predicted rotation velocity at the positions sampled by the PA = 138° data, we found that the data scatter around the model without much evidence of an ordered velocity field. This is not surprising for the three inner positions (2″.5 northeast, nucleus, and 2″.5 southwest), where perturbations can be induced by the radio jet plunging through the ambient gas. For the outermost positions, the observed points present much shallower gradients than expected from the model, with values smaller by 15–50 km s^{-1}. The presence of turbulence on the velocity field across the outer knots has been already noted by other authors and has been explained as effects of the expansion of the ionization front that produces the line emission (Asif et al. 1997) or of cloud-cloud collisions, where the gas streaming in from the leading edge of the bar meets the one trapped in the inner Lindblad resonance orbits (Robinson et al. 1994; Vila-Vilaró et al. 1995).

Therefore, in agreement with previous works, we conclude that the kinematics of the ionized gas in the ENLR of NGC 4151 beyond a distance of about 0.5 kpc is dominated by the general rotation of the galactic disk, with significant perturbations present in the emission-line knots owing to a noncircular or nonplanar velocity component associated with gas turbulence and effects of the ionization front and/or of the presence of the galactic bar.

Under the hypothesis that the emission in the inner 5″ of the NLR of NGC 4151 is produced by gas rotating in the disk of the galaxy, ionized mainly by the central source and kinematically *disturbed* by the interaction with the radio jet, we now assume that the projection of the velocity field in the plane of the sky is determined by the same geometrical parameters (i and Ψ_0) as obtained from the ENLR rotation curve, and use the same procedure as above to fit the FOC f/48 data.

Notice that we do not expect the other parameters of the fit to be the same as or even similar to those obtained for the large-scale rotation, since the high spatial resolution of the *HST* data is sampling the gas whose behavior is governed by the very inner part of the gravitational potential well, while the ENLR gas reacts to the mass distribution on kiloparsec scales.

4.2.2. *The 1996 FOC f/48* [O III] *Data Set*

As before, the full data set was first fitted with A, p, C_0, and $V_{\rm sys}$ as free parameters, while i and Ψ_0 were kept fixed at 21° and 33°.9, respectively, and with $V_{\rm sys}$ having the same value for all data points; then each slit position was separately fitted with the resulting model but allowing $V_{\rm sys}$ to vary. As a double check of the result, we also obtained a fit for each slit position allowing all four parameters to vary and found that the values of $V_{\rm sys}$ for the individual "best" and constrained fits agree well within the errors. As explained in Macchetto et al. (1997), the repositioning of the FOC spectrographic mirror, which moves between flat-field and source exposures, can cause a shift in the zero point of the wavelength scale. If one of the individual data sets is shifted up or down relative to the others, the simultaneous fit to all data will result in a weighted value for $V_{\rm sys}$ and a larger value for A than what would be expected from a uniform wavelength scale. We found a ~10 km s^{-1} shift between the systemic velocity for position PA47_1 and both PA47_2 and PA47_4, obtained in the same orbit, and a ~50 km s^{-1} shift between them and PA47_3, the IntAq spectrum.

The resulting systemic velocity for each slit position was then subtracted from the observed values and the whole data set refitted with A, p, and C_0 as free parameters. Finally, the effect of the initial guess on the parameters was explored as for the ground-based data, and the resulting intervals in the parameters are listed in Table 4, together with the average model ("fit") and the one obtained using only the PA47_1 spectra ("nucleus"), which, as discussed in § 4.2, would be more sensitive to the actual value of C_0. These two models are plotted in Figure 14 as full and dotted lines, respectively. Notice that the points represented as open triangles in Figure 9*a* had been excluded from the final fit. Their projected position corresponds to where the radio jet crosses the slit, and therefore we suspect their high velocity can be due to jet entrainment. If included in the fit, their effect is to increase the total amplitude A of the curve, with

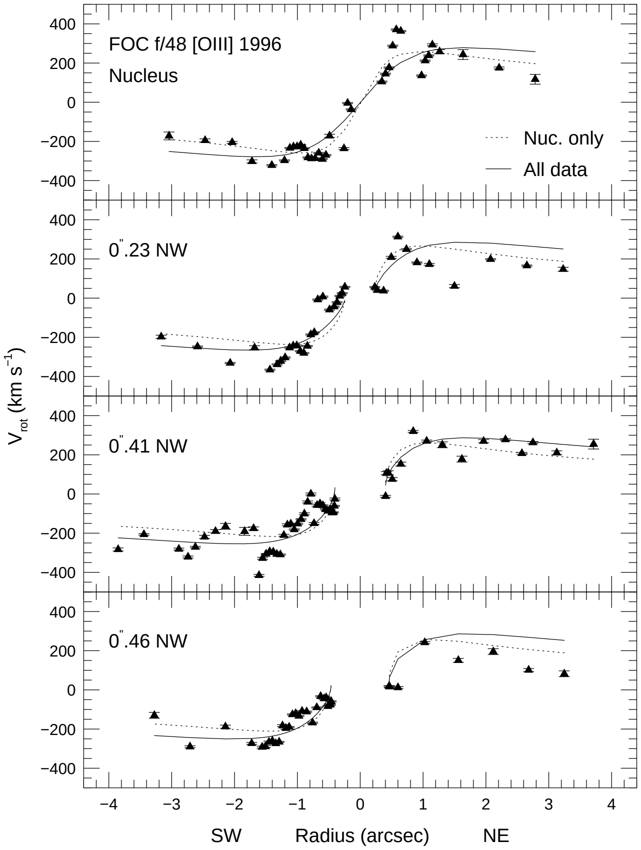

FIG. 14.—Comparison between the 1996 FOC f/48 [O III] λ5007 data set and the best fitting circular rotation curve. The dotted line corresponds to the fit to the nuclear slit position only, and the solid line to the fit obtained using all the four slit positions simultaneously. Notice that the distance scale is now relative to the nucleus.

TABLE 4

MODEL FITTING: *HST* FOC f/48[a]

PARAMETER	1996 [O III] Range	1996 [O III] Fit	1996 [O III] Nucleus	1996 [O II] Range	1996 [O II] Fit	1995 [O II] Range	1995 [O II] Fit
A (km s^{-1})......	1382–1412	1399	986	1434–1508	1478	1133–1175	1157
p	1.499	1.499	1.499	1.499	1.499	1.498–1.50	1.498
C_0 (arcsec)	1.16–1.19	1.18	0.68	1.04 – 1.10	1.07	0.84–0.88	0.86

[a] Using $\Psi = 33°.9$ and $i = 21°$.

little change in the other parameters. The most striking result that emerges from our analysis is that the exponent p of equation (1) changes from 1 to 1.5, which indicates that the potential goes from "dark halo" at the ENLR distances to being dominated by the central mass concentration in the interval $1'' < R < 4''$, with the gas rotation curve presenting an almost Keplerian falloff in this range of radii.

4.2.3. *The 1995 and 1996 FOC f/48* [O II] *Data Sets*

The same procedure as for the 1996 [O III] data set was repeated using the rotation curves obtained from the 1995 and 1996 [O II] λ3727 emission-line measurements. For the 1995 data, only the two innermost positions (PA40_2 and PA40_3) were used. The three data sets give similar results, shown in Table 4 and plotted in Figures 15 and 16 for the [O II] λ3727 1996 and 1995 data, respectively. The northeast side of the 0″.57 SE rotation curve is systematically blueshifted with respect to the model in the inner 1″.2 from the nucleus. This effect can be associated with the expansion of the radio component C5 (see Paper I, Fig. 2), which is localized just northwest of the emission sampled by the slit. The low S/N of the 1995 [O II] λ3727 data does not allow us to completely separate the disturbed components, but one high-velocity component can be seen at the edge of this region in Figure 11.

4.3. *The HST STIS Slitless Data*

In 1997 March, slitless CCD spectra of the NLR of NGC 4151 were taken with the Space Telescope Imaging Spectrometer (STIS) newly installed on board *HST*. A description of the data is given in Hutchings et al. (1998). Although the [O III] λ5007 spectral image has comparable spatial resolution to our data, it suffers from considerable confusion in the inner 2″–3″, where the complex velocity systems lead to an ambiguity between spatial and velocity information. The data are, nevertheless, worthwhile for our purpose, since they contain velocity information extending to larger distances from the nucleus and covering a wider area of the NLR than our spectra. We have used the data given in Table 1 of the Hutchings et al. paper and the same archival WFPC2 [O III] λ5007 image to derive the position relative to the nucleus of the individual clouds identified in their work. We stress that the position ascribed by us to the clouds is uncertain by at least 2 WFPC2 pixels (0″.1). The high-velocity systems detected in the STIS data were excluded and the remaining data within 6″ from the nucleus were fitted using the same procedure as in the previous sections, with $V_{\rm sys}$ set to zero (the velocities in the STIS data are given relative to the nuclear [O III] λ5007 emission).

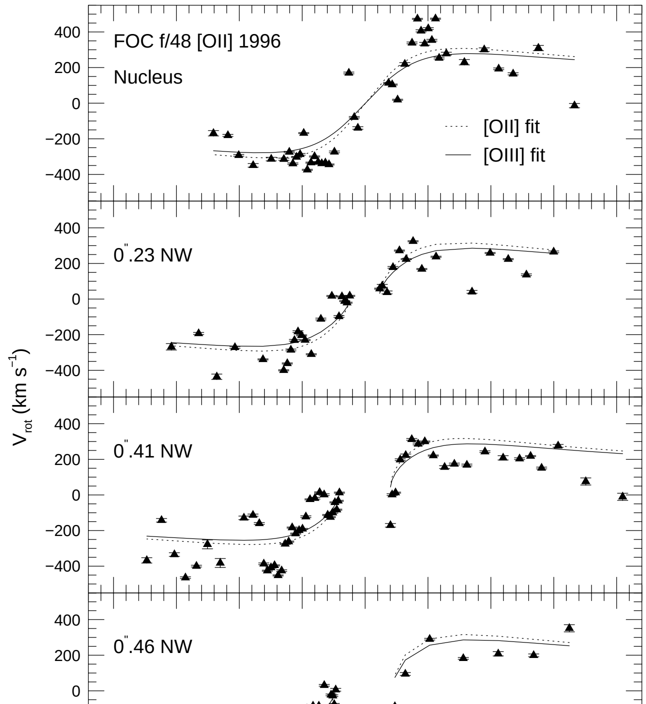

FIG. 15.—Same as Fig. 14 for the 1996 FOC f/48 [O II] λ3727 data set. The solid line corresponds to the fit obtained with the [O III] λ5007 data set (all positions), and the dotted line to the fit obtained using the [O II] λ3727 emission from the four slit positions simultaneously.

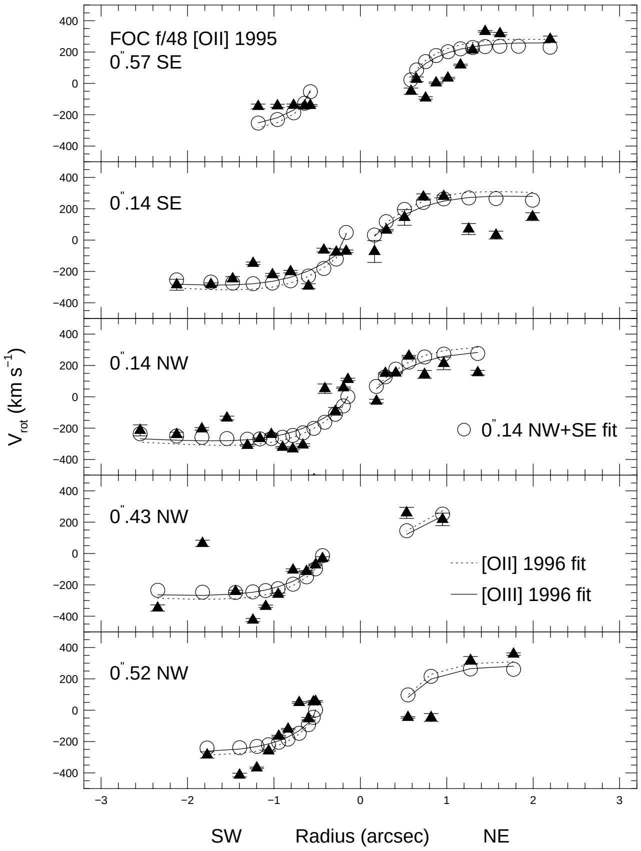

FIG. 16.—Same as Fig. 14 for the 1995 FOC f/48 [O II] λ3727 data set. Here the solid line and dotted lines correspond to the fits obtained with the 1996 [O III] λ5007 and [O II] λ3727 data sets (all positions), respectively, and the open circles represent the fit obtained using the 1995 [O II] λ3727 emission from the two innermost (0″.14 northwest and 0″.14 southeast) slit positions.

The resulting set of parameters is essentially identical to the one obtained for the fit of the FOC f/48 [O III] λ5007 nuclear position alone (model [O III] λ5007 nucleus in Table 4): $A = 998$ km s^{-1}; $p = 1.498$; $C_0 = 0''.75$. The bidimensional representation of these two fits is presented in Figure 17, where the STIS data and corresponding model, and the [O III] λ5007 1996 FOC f/48 data and the nucleus model of Table 4, are shown on the top and bottom panels,

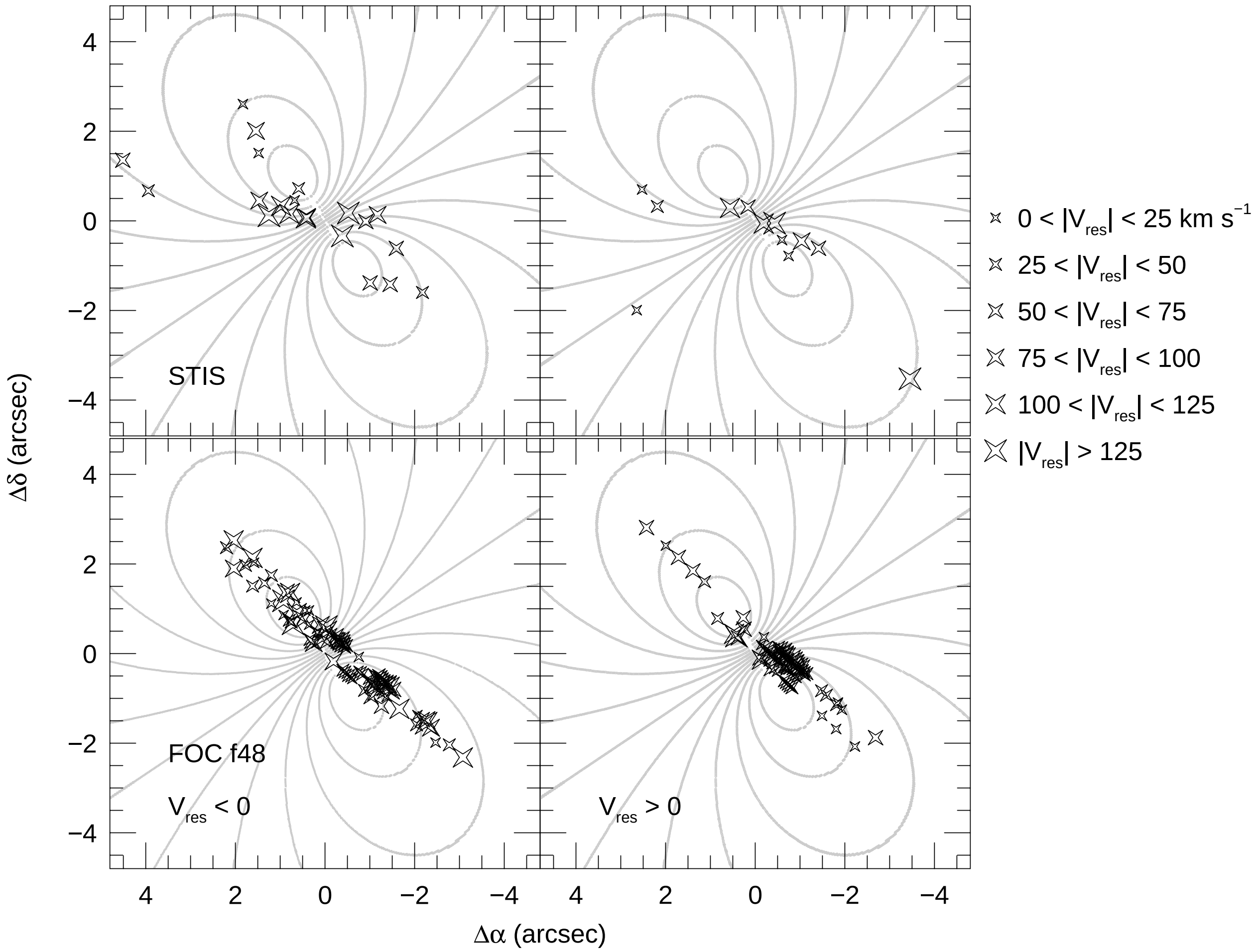

FIG. 17.—Bidimensional representations of the rotation model for the STIS data (*upper panels*) and the [O III] λ5007 nucleus model of Table 4 for the FOC f/48 data (*bottom*). North is up; east to the left. The velocity contours are 0, 40, 80, 120, 160, 200, 240 km s^{-1} to the northeast and the negative equivalents to the southwest. The points are the residuals, defined as $V_{res} = V_{rot} - V_{model}$, negative on the left, and positive on the right panels.

respectively. The velocity contours are 0–240 km s^{-1} in steps of 40 km s^{-1} to the northeast and the negative equivalents to the southwest. The residuals, defined as $V_{res} = V_{rot} - V_{model}$, are negative (the model overestimates the observed velocity) on the left and positive (the model underestimates the observations) on the right panels. There is no preferential distribution of positive and negative residuals as will be expected if the velocity field of the gas was partly due to a large-scale radial component such as a bulk outflow. On the other hand, the largest residuals tend to concentrate around the position of the brightest radio knots, which indicates that the expansion of the hot plasma introduces a significant nonplanar component to the motion of the ambient gas.

5. DISCUSSION

5.1. *The Rotation Curve*

Our INT data confirmed the general result from both H I and other ground-based observations that the gas at large scales is in planar rotation, dominated by the galactic potential. As we approach the nucleus, it is possible to see in both the INT and *HST* data the perturbations introduced by the interaction of the radio jet with the ambient gas superimposed on the rotation component, which, however, still dominates the bulk velocity field.

The combined effect of higher spatial resolution and profile decomposition is apparent when we compare our data with the rotation curve of Robinson et al. (1994), obtained along PA = 51°. The INT curve has a smaller total amplitude in the inner 5″, 180 km s^{-1} instead of ∼350 km s^{-1}. Furthermore, the asymmetry remarked on previously in the ground-based data, where the southwest peak was blueshifted by 200 km s^{-1}, and the northeast redshifted by 50 km s^{-1} with respect to the ENLR, disappears. The line profiles shown in Figure 5 show that such asymmetry is created by the mixing of the high-velocity clouds plus the disk component. The behavior of the line FWHM also indicates that when crossing the NLR boundary, the single-component profile jumps from 420 km s^{-1} to a little over 600 km s^{-1} (see Fig. 16*b* of Robinson et al. 1994), while our "main component" is always below 300 km s^{-1}. This value is also the FWHM for the rotational component in the FOC f/48 data.

One direct consequence of the order-of-magnitude improvement in spatial resolution provided by the FOC f/48 data is that the double-peaked, blueshifted lines previously observed 3″–4″ southwest of the nucleus are not evidence of a systematic bulk outflow but rather a complex profile created by the gas in the disk plus the disturbed component entrained by the radio jet. The presence of both blue- and redshifted high-velocity components in the *HST* spectrum of individual clouds reinforces the argument that the interaction of the jet with the ISM of the host galaxy and the collimated radiation from the central source are key factors in determining the morphology of the NLR, but not its bulk kinematics. Using the simple assumption that the gas in the NLR is in the same plane as the outer ENLR, we have been able to obtain a good parametrization for the rotation curve within 4″ of the central source. Our results indicate that the kinematics of the NLR gas in the interval $30 \lesssim R \lesssim 250$ pc is best represented by a thin disk in rotation around the mass distribution contained within the turnover radius ($\sim 0\farcs5$). The observed velocity of the gas at this radius, taken as purely Keplerian, would imply a mass of $M \sim 10^9\ M_\odot$ within the inner 60 pc.

Although our nuclear spectrum was saturated in the inner $0\farcs3$ and the dispersion of the data points within the turnover radius is rather large, the velocities measured there are *smaller* than farther out, an effect that cannot be ascribed to the spatial PSF and that indicates that the 10^9 $M_\odot$ above is not in a point mass but in an extended distribution. If we assume spherical symmetry for such mass distribution, our first measured velocity points to the northeast and southwest of the nucleus would imply an enclosed mass of $\sim 5 \times 10^8\ M_\odot$ within R (20 pc; $v_{\rm obs} \sim 100$ km s^{-1}) or $\sim 5 \times 10^7\ M_\odot$ within $R \sim 0\farcs15$ (10 pc; $v_{\rm obs} \sim 40$ km s^{-1}), respectively. This value would be an upper limit to any point mass that could be present there. Further observations with higher (or as high) spatial resolution but with better sampling in the inner region of the rotation curve and higher spectral resolution should be able to constrain the nature of the mass distribution further.

The presence of a large central mass concentration was already indicated by the small value of the C_0 parameter when fitting the kinematics the ENLR gas (see § 4.2.1), and the change of behavior of the resulting rotation curve (from flat outside to Keplerian-like in the inner regions) indicates that it dominates the kinematics of the NLR. This is confirmed by a quick analysis of the brightness profile from the archival *HST*/WFPC2 images. Assuming a mass-to-light ratio of 2, we find that the stars contribute at most $\sim 2 \times 10^8\ M_\odot$ to the mass between $0\farcs5$ and 4″. Comparing with a central mass of 5×10^8–$10^9\ M_\odot$ within a $0\farcs5$ radius and considering that the circular velocity scales on the square root of the mass, the presence of an extended (bulge) component would cause the gas in the NLR to deviate from a pure Keplerian rotation curve by $\lesssim$10%–20%. This value is well within the observational scatter of the data, even bearing in mind the considerable uncertainties introduced by the effect of the central source to the brightness profile. Thus even though the mass inside the turnover radius is not a true point source, it is clear why the models yielded such a closely Keplerian value of $p = 1.5$ in our analysis.

The wide-angle ionizing cone model of Pedlar et al. (1993) implies that the common collimation axis of the ionizing cone and the radio jets is not perpendicular to the galactic disk. For $i \sim 21°$ and a bicone opening angle of $\sim 130°$ (see Fig. 8 of Boksenberg et al. 1995), the angle between the collimation axis and the galaxy rotation axis is $\sim 25°$, and the one between the collimation axis and the line of sight, $\sim 40°$. Our model for the kinematics of the gas in the inner NLR indicates that it is still rotating in the plane of the galaxy even at distances of a few tens of parsecs from the nucleus and therefore is not directly related to the symmetry axis of the AGN itself. Such a lack of common orientation is also indicated by the radio observations of Weymann et al. (1997) at subparsec scales and by the Fe Kα profile presented by Yaqoob et al. (1995). If it is assumed that the Fe Kα line is produced in the accretion disk, the models indicate that the structure within $10^3\ r_g$, the gravitational radius of the black hole, is essentially face-on. A similar situation is seen in the recent *HST* infrared observations of Centaurus A (Schreier et al. 1998), where the gas disk structure at ~ 20 pc scales is oriented along the major axis of the bulge, an indication that its geometry is set by the galaxy gravitational potential rather than by the symmetry of the AGN and its jet.

5.2. *Evidence for Rotation in Other Objects*

Two other AGNs, NGC 1068 and Mrk 3, have been spectroscopically studied with *HST* with enough detail and spatial resolution to carry out an analysis similar to that in this paper. While in the first object we also observe strong but localized perturbations induced by the interaction of the radio jet with the ambient gas superimposed in a more general pattern characteristic of ordered rotation (Axon et al. 1997), in Mrk 3 the gas motions in the region cospatial with the radio jet are clearly dominated by the expansion of the cocoon of hot gas shocked and heated by the radio ejecta (Capetti et al. 1999). Such observations are in agreement with Nelson & Whittle (1996) results, where it was argued that the correlations between the stellar velocity dispersion and the [O III] profile in a large sample of ground-based observations of Seyfert galaxies indicate that the motions in the NLR are predominantly gravitational in nature, with objects with linear radio sources presenting broader [O III] lines.

Evidence for an underlying rotational component is also found in ground-based studies of several other objects, such as NGC 1365 (Hjelm & Lindblad 1996), NGC 3516 (Mulchaey et al. 1992; Arribas et al. 1997), and NGC 2992 (Márquez et al. 1998; Allen et al. 1999), with a general trend for the low-ionization gas to be a better tracer of the disk component, while the high-ionization gas presents more deviant behavior, usually associated with outflow.

We remark that all these studies used the centroid of the emission lines, rather than the individual components, and, until now, the observations did not have enough spatial resolution to separate the individual clouds and to show whether the often noted double-peaked profile is seen everywhere, which implies that the outflow is actually a wind, or is localized, as expected when the gas is entrained by the radio jet. The observations are also naturally biased toward the brighter emission line knots, which are more likely to be disturbed, either by the interaction with the radio jets, tidal effects, or even the central source radiation. Obtaining good S/N data of the central regions of other AGN with high spatial resolution and even moderate spectral resolution can prove to be a useful technique for detecting the undisturbed gas and probing the nature of the central potential. Since stellar dynamical methods are rendered impotent, as the absorption lines in Seyfert spectra are inevitably filled in by the featureless continuum, this approach may provide the only means of directly determining the central object (black hole) mass in currently active nuclei.

A potentially interesting follow-up of such studies is that, if the mass of the central object M is determined using the NLR gas kinematics, the presence of continuum variability can, in principle, provide an estimate for another key missing piece of information on AGN models, the accretion rate $\dot{M}$. Using a very simple steady state, irradiated blackbody approximation for the thermal structure of the accretion disk, Peterson et al. (1998) presented evidence of a correlation between the product ($M\dot{M}$) and the time delay between different continuum wave bands in NGC 7469 (Wanders et al. 1997; Collier et al. 1998), the only source in which significant delays have been detected. If such a correlation is found to hold for other nuclei, the two methods above would provide totally independent estimates for each of the quantities. However, viscous dissipation timescales are too long to reconcile with the observed continuum lags, which forces consideration of X-ray–irradiated or composite models (Sincell & Krolik 1998; Collier et al. 1999). Therefore, with an independent measure of the central object mass, obtaining $\dot{M}$ would be dependent on further development of the accretion disk theory itself, and to obtain it using AGN continuum variability would make it necessary to carry on high sampling rate, simultaneous multiwavelength campaigns on other nearby active galaxies.

6. SUMMARY

We can summarize the main results of our study of both *HST* and ground-based long-slit spectra of the inner and extended NLR of NGC 4151 as follows:

1. By decomposing the [O III] λ5007 line profile in multiple Gaussian components, we were able to trace the main kinematic component of the ENLR across the nuclear region, connecting smoothly the emission gas system with the large-scale rotation defined by H I observations.

2. Individual clouds in the NLR ($R < 4''$) are observed to be kinematically disturbed by the interaction with the radio jet, but underlying these perturbations the cloud system is moving in a pattern compatible with disk rotation. High-velocity components (up to ± 1000 km s^{-1}, relative to systemic) and broad (FWHM up to 1800 km s^{-1}) bases are detected in the [O III] λ5007 profile of the brightest clouds. Such regions are invariably at the edge of the radio knots, and this association, together with the overall morphology of the velocity field, leads us to propose that the main kinematic system in the inner region of NGC 4151 is still rotation in the plane of the disk, *disturbed but not defined* by the interaction with the radio jet and the AGN emission.

3. Fitting a simple expression for planar rotation to the data, we find that the ENLR gas ($R > 4''$) presents a kinematic behavior consistent with and well represented by rotation in the galactic disk, with characteristics similar to other normal spiral systems. We obtain $i = 21^\circ$, and $\Psi_0 = 34^\circ$–43° for the inclination to the line of sight and position angle of the line of nodes of the disk, respectively. The velocity field of external knots at $R \sim 6''$ and $20''$ transverse to the radial direction presents evidence of nonplanar or noncircular movements, probably associated with gas turbulence and streaming motions along the bar.

4. Using the same projection angles as obtained for the ENLR, the NLR emission component believed to represent the continuation of the disk velocity field was also found to be consistent with planar rotation, although disturbed by the jet, as expected. However, while the velocity field of the extended ENLR gas is dominated by the potential of the galactic bulge, presenting a flat curve at large distances, we find that the behavior of the gas in the inner NLR is best represented by a Keplerian-like potential, with the kinematics of the gas up to $4''$ dominated by the $\sim 10^9\ M_\odot$ mass concentration located within the turnover radius of the rotation curve, located at $\sim 0''.5$. Our measurements inside the turnover radius imply that this is an extended distribution rather than a point mass, and, if spherical symmetry is assumed, the innermost observed velocity still not affected by the spatial PSF gives a $5 \times 10^7\ M_\odot$ mass concentrated within a radius of about 10 pc.

C. W. thanks the Space Telescope Science Institute for the hospitality during the last 2 yr and acknowledges the financial support from the Brazilian institution CNPq through a postdoctoral fellowship and from ESA. We also thank the referee, R. Antonucci, for his very thorough reading of this paper.

REFERENCES

Allen, M. G., Dopita, M. A., Tsvetanov, Z. I., & Sutherland, R. S. 1999, ApJ, 511, 686

Arribas, S., Mediavilla, E., García-Lorenzo, B., & Del Burgo, C. 1997, ApJ, 490, 227

Asif, M. W., Unger, S. W., Pedlar, A., Mundell, C. G., Robinson, A., & Walton, N. A. 1997, MNRAS, 284, 15P

Axon, D. J., Marconi, A., Capetti, A., Macchetto, F. D., Schreier, E., & Robinson, A. 1998, ApJ, 496, L75

Bertola, F., Bettoni, D., Danziger, J., Sadler, E., Sparke, L., & de Zeeuw, T. 1991, ApJ, 373, 369

Boksenberg, A. 1972, in ESO/CERN Conference on Auxiliary Instrumentation for Large Telescopes, ed. S. Lautsten & A. Reiz (Geneva: ESO), 295

Boksenberg, A., & Burgess, D. E. 1973, in Astronomical Observations with Television-Type Sensors, ed. J. W. Glaspey & G. A. H. Walkers (Vancouver, B.C.: Best Printer), 21

Boksenberg, A., et al. 1995, ApJ, 440, 151

Bosma, A., Ekers, R. D., & Lequeux, J. 1977, A&A, 57, 97

Capetti, A., Axon, D. J., Marconi, A., Macchetto, F. D., & Winge, C. 1999, ApJ, 516, 000

Collier, S., et al. 1998, ApJ, 500, 162

Collier, S., Horne, K., Wanders, I., & Peterson, B. M. 1999, MNRAS, 302, L24

Crenshaw, D. M., et al. 1996, ApJ, 470, 322

Espey, B. R., Kriss, G. A., Krolik, J. H., Zheng, W., Tsvetanov, Z., & Davidsen, A. F. 1998, ApJ, 500, L13

Evans, I. N., Tsvetanov, Z., Kriss, G. A., Ford, H. C., Caganoff, S., & Koratkar, A. P. 1993, ApJ, 417, 82

Hjelm, M., & Lindblad, P. O. 1996, A&A, 305, 727

Hutchings, J. B., et al. 1998, ApJ, 492, L115

Kaspi, S., et al. 1996, ApJ, 470, 336

Knop, R. A., Armus, L., Larkin, J. E., Matthews, K., Shupe, D. L., & Soifer, B. T. 1996, AJ, 112, 81

Kriss, G. A., Davidsen, A. F., Zheng, W., Kruk, J. W., & Espey, B. R. 1995, ApJ, 454, L7

Macchetto, F. D., Marconi, A., Axon, D. J., Capetti, A., Sparks, W. B., & Crane, P. 1997, ApJ, 489, 579

Márquez, I., Boisson, C., Durret, F., & Petitjean, P. 1998, A&A, 333, 459

Mediavilla, E., & Arribas, S. 1995, MNRAS, 276, 579

Mediavilla, E., Arribas, S., & Rasilla, J. L. 1992, ApJ, 396, 517

Mulchaey, J. S., Tsvetanov, Z., Wilson, A. S., & Pérez-Fournon, I. 1992, ApJ, 394, 91

Nelson, C. H., & Whittle, M. 1996, ApJ, 465, 96

Nota, A., et al. 1996, FOC Instrument Handbook, version 7.0 (Baltimore: STScI)

Pedlar, A., Howley, P., Axon, D. J., & Unger, S. W. 1992, MNRAS, 259, 369

Pedlar, A., Kukula, M. J., Longley, D. P. T., Muxlow, T. W. B., Axon, D. J., Baum, S., O'Dea, C., & Unger, S. W. 1993, MNRAS, 263, 471

Penston, M. V., et al. 1990, A&A, 236, 53.

Pérez, E., González-Delgado, R., Tadhunter, C., & Tsvetanov, Z. 1989, MNRAS, 241, 31P

Pérez, E., et al. 1999, in preparation

Peterson, B. M., Wanders, I., Horne, K., Collier, S., Alexander, T., Kaspi, S., & Maoz, D. 1998, PASP, 110, 660

Pringle, J. E. 1997, MNRAS, 292, 136

Robinson, A., et al. 1994, A&A, 291, 351

Rubin, V. C., Burstein, D., Ford, W. K., Jr., & Thonnard, N. 1985, ApJ, 289, 81

Schreier, E. J., et al. 1998, ApJ, 499, L143

Schulz, H. 1987, A&A, 178, 7

———. 1990, AJ, 99, 1442

Simkin, S. M. 1975, ApJ, 200, 567

Sincell, M. W., & Krolik, J. H. 1998, ApJ, 496, 737

Shortridge, K. 1993, in ASP Conf. Ser. 52, Astronomical Data Analysis Software and Systems II, ed. R. J. Hanisch, R. J. V. Brissenden, & J. Barnes (San Francisco: ASP), 219

Steffen, W., Gómez, J. L., Raga, A. C., & Williams, R. J. R. 1997a, ApJ, 491, L73

Steffen, W., Gómez, J. L., Williams, R. J. R., Raga, A. C., & Pedlar, A. 1997b, MNRAS, 286, 1032

Taylor, D., Dyson, J. E., & Axon, D. J. 1992, MNRAS, 255, 351

Ulvestad, J. S., Roy, A. L., Colbert, E. J. M., & Wilson, A. S. 1998, ApJ, 496, 196

van der Kruit, P. C., & Shostak, G. S. 1984, A&A, 134, 258

Vila-Vilaró, B., et al. 1995, A&A, 302, 58

Wanders, I., et al. 1997, ApJS, 113, 69

Warwick, R. S., et al. 1996, ApJ, 470, 349

Weymann, R. J., Morris, S. L., Gray, M. E., & Hutchings, J. B. 1997, ApJ, 483, 717

Wilkins, T. W., & Axon, D. J. 1992, in ASP Conf. Ser. 25, Astronomical Data Analysis Software and Systems I, ed. D. Worral, C. Biemesderfer, & J. Barnes (San Francisco: ASP), 427

Winge, C., Axon, D. J., Macchetto, F. D., & Capetti, A. 1997, ApJ, 487, L121 (Paper I)

Yaqoob, Y., Edelson, R., Weaver, K. A., Warwick, R. S., Mushotzky, R. F., Serlemitsos, P. J., & Holt, S. S. 1995, ApJ, 453, L81

Yoshida, M., & Ohtani, H. 1993, PASJ, 45, 407